Retrolaminar Demyelination of Structurally Intact Axons in Nonhuman Primate Experimental Glaucoma

Priya Chaudhary,[1,2] Howard Lockwood,[1,2] Cheri Stowell,[1,2] Eric Bushong,[3] Juan Reynaud,[1,2] Hongli Yang,[1,2] Stuart K. Gardiner,[2] Galen Wiliams,[1,2] Imee Williams,[1,2] Mark Ellisman,[3] Nick Marsh-Armstrong,[4] and Claude Burgoyne[1,2]

[1]Optic Nerve Head Research Laboratory, Legacy Devers Eye Institute, Legacy Research Institute, Portland, Oregon, United States
[2]Discoveries in Sight, Devers Eye Institute, Legacy Research Institute, Portland, Oregon, United States
[3]National Center for Microscopy & Imaging Research, UCSD, La Jolla, California, United States
[4]Department of Ophthalmology, University of California, Davis, California, United States

Correspondence: Claude F. Burgoyne, Optic Nerve Head Research Laboratory, Devers Eye Institute, Legacy Research Institute, 1225 NE 2nd Avenue, Portland, OR 97232, USA;
cfburgoyne@deverseye.org.

Received: November 2, 2023
Accepted: January 28, 2024
Published: February 26, 2024

Citation: Chaudhary P, Lockwood H, Stowell C, et al. Retrolaminar demyelination of structurally intact axons in nonhuman primate experimental glaucoma. *Invest Ophthalmol Vis Sci.* 2024;65(2):36. https://doi.org/10.1167/iovs.65.2.36

Purpose. To determine if structurally intact, retrolaminar optic nerve (RON) axons are demyelinated in nonhuman primate (NHP) experimental glaucoma (EG).

Methods. Unilateral EG NHPs ($n = 3$) were perfusion fixed, EG and control eyes were enucleated, and foveal Bruch's membrane opening (FoBMO) 30° sectoral axon counts were estimated. Optic nerve heads were trephined; serial vibratome sections (VSs) were imaged and colocalized to a fundus photograph establishing their FoBMO location. The peripheral neural canal region within $n = 5$ EG versus control eye VS comparisons was targeted for scanning block-face electron microscopic reconstruction (SBEMR) using micro–computed tomographic reconstructions (µCTRs) of each VS. Posterior laminar beams within each µCTR were segmented, allowing a best-fit posterior laminar surface (PLS) to be colocalized into its respective SBEMR. Within each SBEMR, up to 300 axons were randomly traced until they ended (nonintact) or left the block (intact). For each intact axon, myelin onset was identified and myelin onset distance (MOD) was measured relative to the PLS. For each EG versus control SBEMR comparison, survival analyses compared EG and control MOD.

Results. MOD calculations were successful in three EG and five control eye SBEMRs. Within each SBEMR comparison, EG versus control eye axon loss was −32.9%, −8.3%, and −15.2% (respectively), and MOD was increased in the EG versus control SBEMR ($P < 0.0001$ for each EG versus control SBEMR comparison). When data from all three EG eye SBEMRs were compared to all five control eye SBEMRs, MOD was increased within the EG eyes.

Conclusions. Structurally intact, RON axons are demyelinated in NHP early to moderate EG. Studies to determine their functional status are indicated.

Keywords: serial block-face scanning electron microscopy, nonhuman primate, monkey, glaucoma, lamina cribrosa, myelin, demyelination

A large literature provides evidence for a primary insult to the retinal ganglion cell (RGC) axon within the optic nerve head (ONH) tissues in mouse,[1,2] rat,[3] nonhuman primate (NHP),[4–6] and human[7] glaucoma. We have previously reported that the optic neuropathy of NHP experimental glaucoma (EG)[8] is, in part, defined by profound deformation and remodeling of the ONH connective tissues, which include the lamina cribrosa, perineural canal (pNC) sclera, and retrolaminar dural sheath.[9–15] We have separately argued that the optic neuropathy of human glaucoma is similarly defined by these same connective tissue phenomena[16,17] based on a growing group of in vivo optical coherence tomography (OCT)[18–25] studies.

However, at present, the mechanisms by which ONH connective tissue deformation and remodeling contribute to RGC axon compromise within the ONH tissues remain unknown. To study these mechanisms, we recently introduced a novel, full tissue section, quantitative immunohistochemistry (qIHC) method that allowed anatomically consistent EG versus control eye detection of alterations in myelin-related proteins (2′,3′-cyclic nucleotide 3′-phosphodiesterase and myelin basic protein) within the immediate retrolaminar optic nerve (RON) in NHP early to moderate EG. In that study, our data also suggested that ionized calcium binding adaptor molecule 1 (Iba1)–positive and NucBlue pixel-cluster densities were increased within both the laminar and retrolaminar regions in the same EG versus control eyes.

Axons are conventionally described to be myelinated behind the lamina but unmyelinated within and anterior to the lamina. Radius and Pederson[26] reported scattered demyelination in axons behind the lamina in two NHP EG eyes with "early" glaucomatous damage as assessed

Investigative Ophthalmology & Visual Science

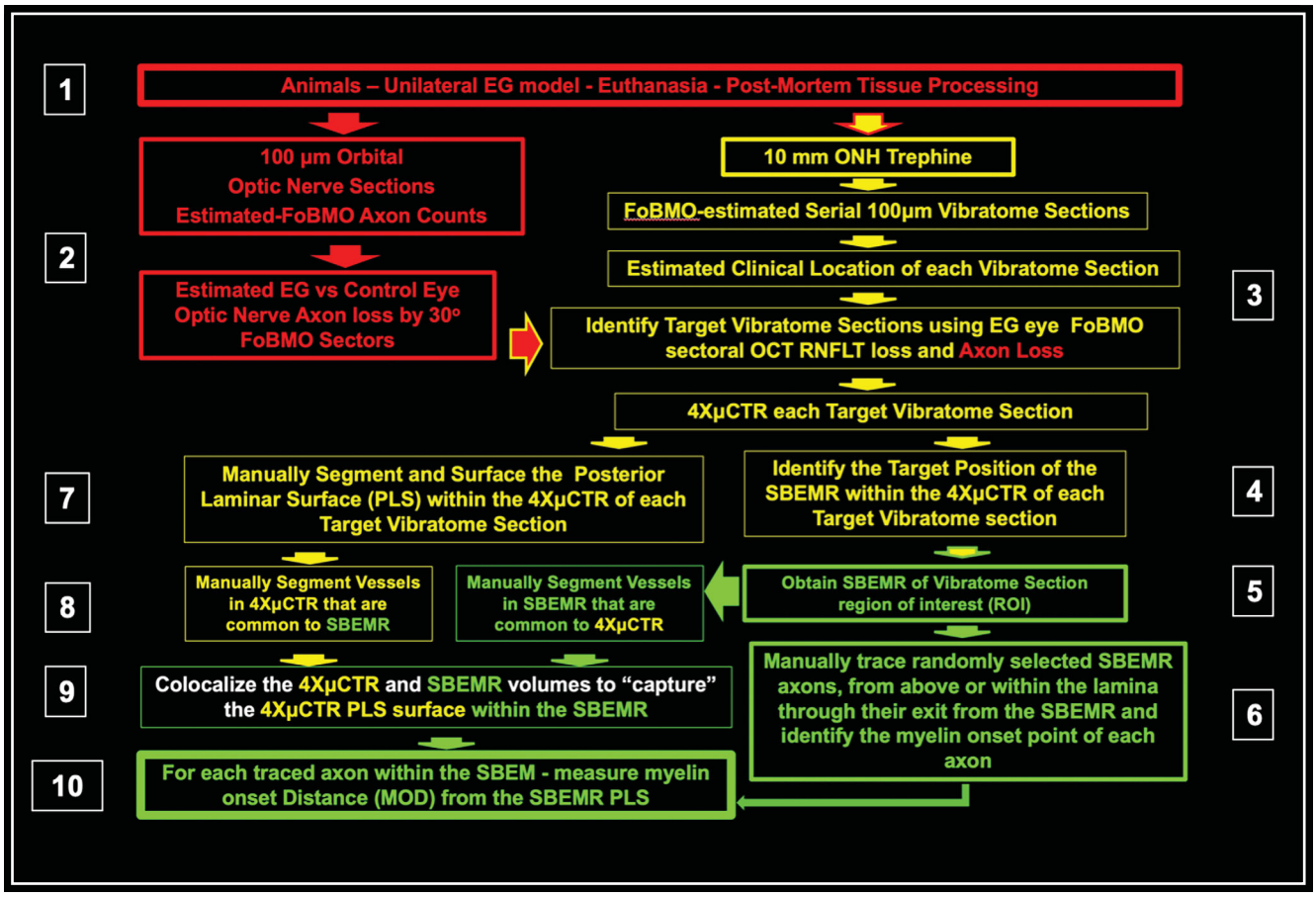

Figure 1. Schematic overview of the three components of our method illustrating their relationships to one another. The first 10 subsections of the Methods section are organized relative to the 10 subgroups (*white numbers*) of this schematic. *Red outlined boxes* refer to animals and initial tissue processing through RON axon counting (hereafter axon counting). *Yellow boxes* refer to steps that focus on the 4XµCT digital reconstruction (4XµCTR) of a target vibratome tissue section. *Green boxes* refer to steps that occur within the SBEMR that is obtained from the peripheral ONH neural canal region of a target vibratome section.

by cup/disc ratio and global RON axon count estimates. While secondary disruption of RON myelin following the loss of RGC axons would be expected in any form of optic neuropathy,[27–33] in the present report, we seek evidence to support the hypothesis that demyelination of structurally intact axons is present early in the optic neuropathy of unilateral NHP EG. Such a finding would be important because follow-up studies could then test the hypothesis that these structurally intact axons were also functionally intact through the bilateral intravitreal injection of markers for axoplasmic transport and flow prior to sacrifice.[4,5,34–37] The detection of demyelinated but functionally intact axons in NHP early EG would be additionally important because it would create a logic for trying some of the many neuroprotective therapeutic interventions developed for treating demyelination in other diseases[38–45] in human ocular hypertension and glaucoma.

Our study employs a series of novel methodologies (Fig. 1 and Table 1) and uses the ONH tissues from $n = 3$ NHPs with unilateral EG (Table 2) to create a total of $n = 5$ anatomically consistent EG versus control eye, serial block-face scanning electron microscopy reconstruction (SBEMR) comparisons. For each comparison, axons were traced, and the onset of myelin was noted and measured relative to an estimated posterior lamina surface (PLS) in each EG and control eye SBEMR (comparisons C1 through C5; Table 3). As in our

Table 1. Acronyms and Definitions

Acronym	Definition
BMO	Bruch's membrane opening
Control	Control eye of a unilateral EG NHP
EG	Experimental glaucoma and the EG eye of a unilateral EG NHP
EM	Electron microscopy
FoBMO	Axis defined by the foveal and BMO centroids (see Fig. 3)
ID	Identification—as in study subject "ID" number
IOP	Intraocular pressure
mm	Millimeter
NHP	Nonhuman primate
nm	Nanometer
OCT	Optical coherence tomography
ONH	Optic nerve head
RNFLT	Retinal nerve fiber layer thickness (as measured by OCT)
ROI	Region of Interest
Sector	ONH FoBMO 30° (clock-hour) sectors (see Figs. 2 and 3)
SBEM	Scanning block-face electron microscopy (referring to the method)
SBEMR	SBEM reconstruction (referring to an individual 3D volume)
µCT	Microscopic X-ray computed tomography (referring to the method)
µCTR	µCT reconstruction (referring to an individual 3D volume)
µm	Micron

Table 2. Animal, Demographic, IOP, Global OCT EG Eye RNFLT Loss and Global Orbital Optic Nerve Axon Alterations at Euthanasia

Animal#	Sex	Age at Euthanasia, y (mo)	Weight (kg)	Eye	EG or C	Baseline Mean IOP* (mm Hg)	Postlaser Mean IOP (mm Hg)	Postlaser Peak IOP (mm Hg)	IOP at Euthanasia† (mm Hg)	EG Eye: Cumulative IOP Insult‡ (mm Hg/d)	EG Eye: Global % RNFLT Loss at Euthanasia§ (mm)	Global Axon Counts	EG vs. C: Global % Axon Count Difference (EG – C)/C	EG vs. C: Global % Axon Density Difference (EG – C)/C	EG vs. C: Global % Axon Size Difference (EG – C)/C
NHP1	M	3 (5)	6.8	OD	EG	11.66	30.54	44.6	23.67	994	31.2 | 31.4	578,105	−54.1	−53.4	−31.2
				OS	C	9.44	11.12	14.6	9.3			1,259,345			
NHP2	M	24 (6)	12.3	OD	EG	12.88	17.03	30	16	415.8	11.1 | 9.5	1,082,035	−10.9	−16.4	6.5
				OS	C	12.95	12.15	14.3	13			1,214,938			
NHP3	F	3 (3)	5.7	OS	EG	11.11	13.31	20	7.67	150.3	5 | 4.6	1,064,966	−5.5	1.6	−14.7
				OD	C	11.88	12.2	16.3	8			1,126,698			

C, control; F, female; M, male.
* Baseline mean IOP C/EG (mm Hg): average of all prelaser IOP measurements.
† IOP at euthanasia: IOP on necropsy table prior to sacrifice.
‡ Cumulative IOP insult: difference between EG versus C eye area under the postlaser IOP curves expressed in mm Hg × days.
§ EG eye % RNFLT loss at euthanasia: data are EG/C at euthanasia (left) and EG eye at euthanasia / EG eye at baseline (right).

Table 3. Animal-Specific EG Versus Control (C) Eye SBEMR Data by Comparison Number

EG vs. C SBEMR Comparison Number*	NHP Study ID	EG Eye: SBEMR ID†	Control Eye: SBEMR ID†	Sampled ONH FoBMO 30° Sector‡	EG vs. C: Sectoral % RNFLT Difference (EG – C)/C	EG vs. C: Peripheral Neural Canal % Axon Count Difference (EG – C)/C	EG vs. C: Peripheral Neural Canal % Axon Density Difference (EG – C)/C	EG vs. C: Peripheral Neural Canal % Axon Size Difference (EG – C)/C
C1§	NHP1	Bhx8†	Bhz2†	Temporal (sector 9)	−8	−32.9	−23.8	−36.2
C2§	NHP2	Bif11†	Bii3†	Nasal (sector 3)	0	−8.3	0.9	0.1
C3§	NHP2	Big4†	Bii5†	Temporal-inferior (sector 8)	−20	−15.2	−18.6	−14.7
C4||	NHP3	Not available¶	Bin11†,#	Nasal (sector 3)	−7	−12.8	−16.1	−35.4
C5§	NHP1	Not available**	Bia8†,#	Inferior-temporal (sector 7)	−38	−74.5	−75.9	−47.8

* We report a total of $n = 3$ EG versus control eye SBEMR comparisons. In two additional comparisons (C4 and C5), axon tracing in the EG eye was not possible (see Methods), but for both comparisons, control eye SBEMR data were used in a subset of analyses (see Methods). See Table 1 for acronym definitions. $n = 5$ EG versus control eye SBEMR comparisons were planned; for comparisons 4 and 5, EG eye data were not available (see Methods).
† Unique four-digit identifier for each SBEMR.
‡ Each EG versus control eye SBEMR comparison used tissue from the same 30° ONH sector of both eyes—see Figures 2 and 3 for sectoral names and locations.
§ Details for each C1, C2, C3, and C5 SBEMR: volume size, 200 × 200 × 50 µm; acquired pixel size, 10 × 10 nm; sectioning interval, 50 nm; acquired voxel size, 10 × 10 × 50 nm; IMOD analysis voxel size after 5 × 5 transverse pixel binning, 50 × 50 × 50 nm.
|| Details for both C4 SBEMRs: volume size, 200 × 400 × 75 µm; acquired and IMOD analysis voxel sizes identical to C1, C2, C3, and C5 SBEMRs (above).
¶ EG eye data not available because an SBEM gap in acquisition did not allow axon tracing (see Methods).
# While EG eye data were not available for this comparison, the control eye data were used in a subset of analyses.
** EG eye data not available because the extent of damage was beyond early to moderate EG and did not allow axon tracing (see Methods).

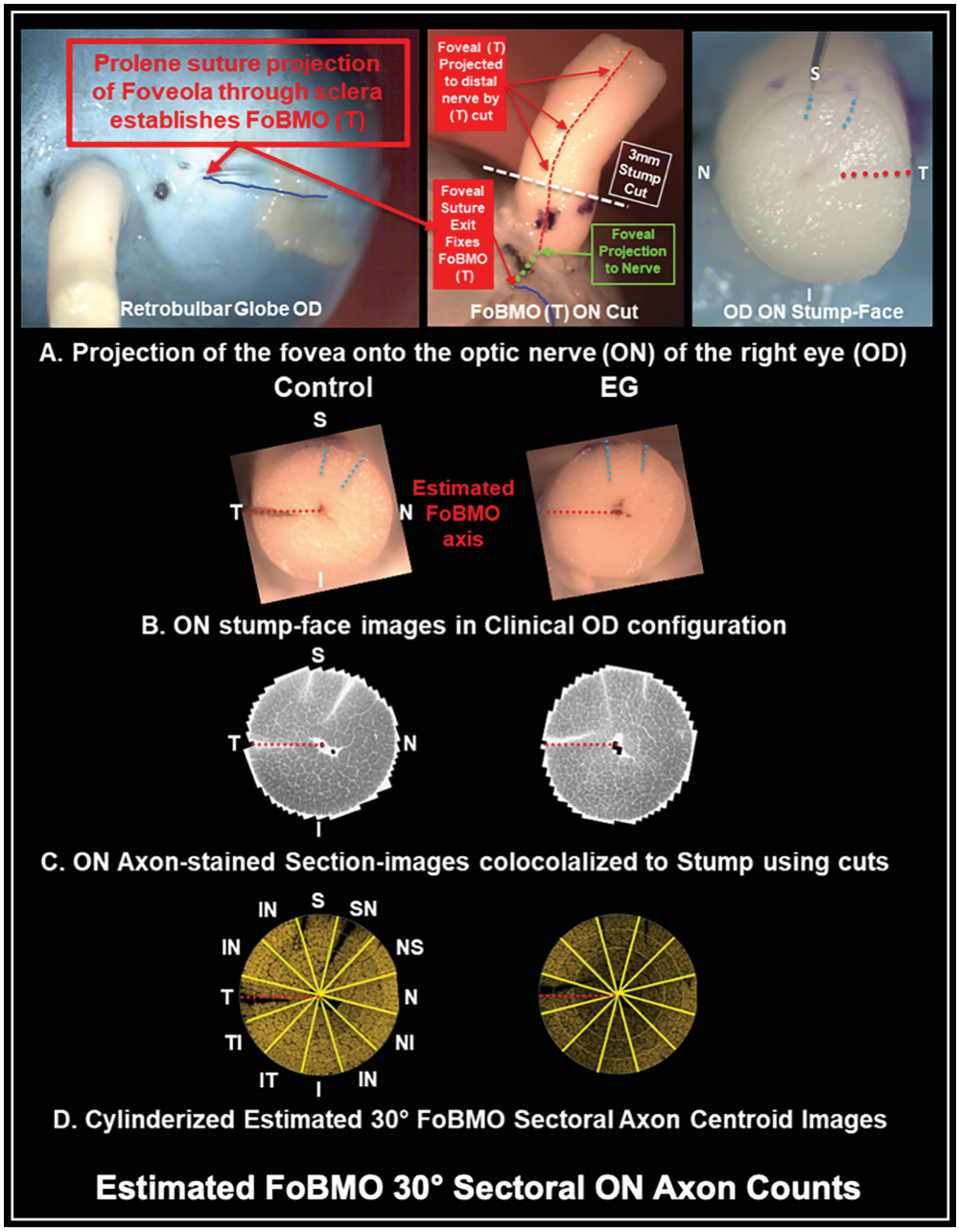

Figure 2. Post-mortem tissue processing part 1: estimated FoBMO optic nerve cuts and orbital optic nerve tissue processing for later axon count, density, and size calculations within each study eye. (**A**) *Left and middle*: The dural sheath of a right eye is dissected away from the orbital nerve as well as its insertion into the sclera so as to reveal the optic nerve exit from the posterior scleral canal. The fovea is projected to the posterior scleral surface by passing a 10-prolene suture (shown in *blue*) on a straight needle (not shown) through the fovea and sclera. *Middle*: The posterior scleral projection of the fovea is visually projected along the posterior scleral surface (*green dotted line*) to the temporal (T) midline of the orbital optic nerve and is then extended along the nerve by a (T) cut followed by two additional superior cuts (also along the full extent of the optic nerve), which are then documented on the 3-mm ON stump face (*right*). (**B**) Stump-face images for the control and EG eye in OD clinical configuration with the temporal cut serving as the estimated FoBMO axis. (**C**) ON axon-stained tissue section images after colocalization to the stump-face images allowing the FoBMO (T) axis to be estimated prior to automated counting (as previously published; see Methods). (**D**) Cylinderization of each axon within their respective axon centroid image allows EG versus control comparisons to occur in eyes in which the EG and control eye ON sections are of different size and shape. See Methods for additional details. FoBMO sectoral acronyms (**D**): I, inferior; IN, inferior-nasal; IT, Inferior-temporal; N, nasal; NI, nasal-inferior; NS, nasal-superior; S, superior; SN, superior-nasal; ST, superior-temporal; T, temporal; TI, temporal-inferior; TS, temporal-superior. See Table 1 for additional acronym definitions.

prior qIHC report,[46] in the present study, we use the phrase "anatomically consistent EG versus control eye comparisons" to mean that all cross-sectional and longitudinal OCT data, all post-mortem RON axon counts, and each EG versus control eye SBEMR comparison are made within anatomically consistent EG and control eye foveal Bruch's membrane opening (FoBMO) 30° sectoral ONH regions (Figs. 2–4). It additionally means that each SBEMR comparison has

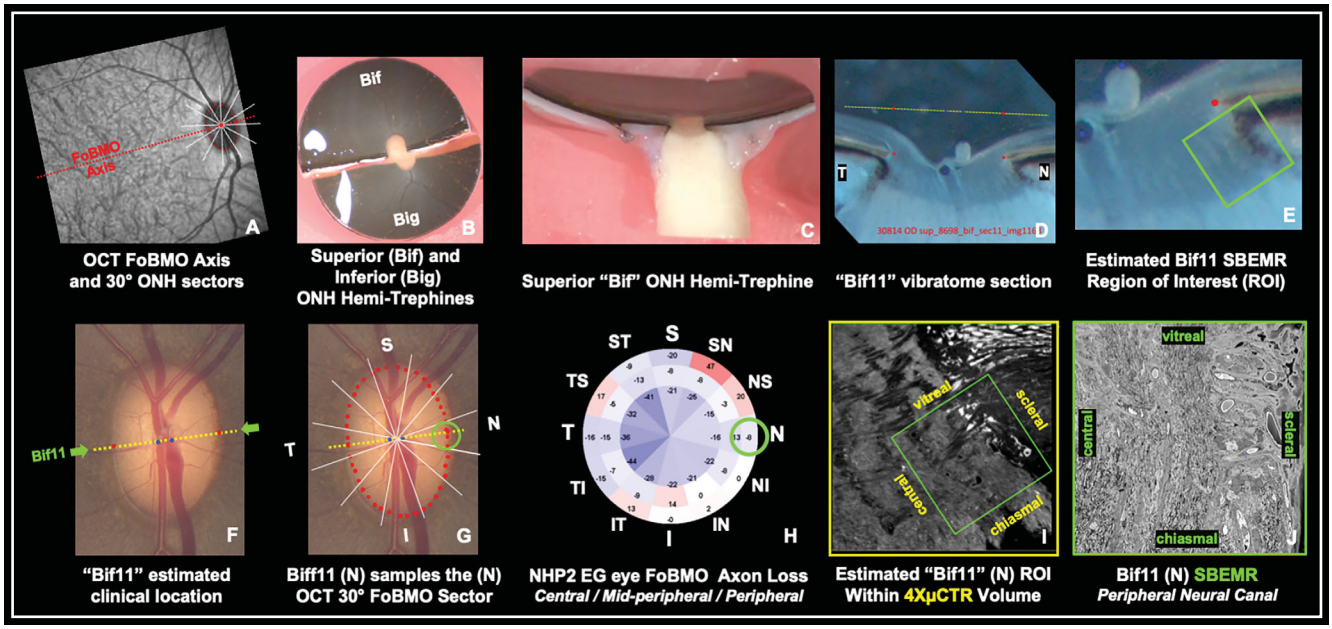

Figure 3. Post-mortem tissue processing part 2: controlling the anatomic location of the NHP2 Bif11 EG eye nasal (N) (Table 2) SBEMR so as to sample the peripheral-most axon bundles within the laminar and RON regions of the nasal (N) FoBMO 30° sector (ON axon loss 8.3%). (**A–H**) The clinical and anatomic locations of the SBEMR are shown. (**A**) The infrared (IR) image acquired at the time of OCT acquisition showing the FoBMO axis (*red dotted line*) extending from the OCT-detected center of the fovea through the OCT-detected BMO (*small red dots*) and centroid (*large red dot*). The OCT FoBMO ONH 30° sectors (*white lines*) are also shown. (**B**) Manual transection of the 10.0-mm ONH trephine along a line approximating the FoBMO axis into superior (tissue number "Bif") and inferior (tissue number "Big") hemi-trephines for serial 100-μm vibratome sectioning. (**C**) Cut-face of the superior hemi-trephine. (**D**) For each vibratome section, BMO points (*red dots*) and vessel locations (*blue dots*) are used to identify the section's location within a clinical fundus photo (*green arrows* in **F**). (**E**) Closeup of the nasal side of the Bif11 vibratome section in **D**, in which the SBEMR ROI has been tentatively identified (*white square*). (**F**) Each individual vibratome section is colocalized to the clinical ONH photograph using the histologic BMO (*red*) and vessel (*blue*) points identified in **D** (see Methods). (**G**) The OCT FoBMO 30° sectors are imposed onto the fundus photo after it has been colocalized to the OCT IR, allowing the FoBMO sectoral location of the SBEMR to be estimated. (**H**) Estimated FoBMO EG eye axon count differences from control (−8% for the peripheral subsector of the [N] 30° sector [*green circle*]). The 30° sectoral acronyms are defined at the end of this legend. (**I**) A single optical section image from a 4× microscopic x-ray computed tomographic reconstruction (μCTR) of the vibratome section is used to finalize the x-y-z location (*green box*) of the 200 × 200 × 50-μm SBEMR within the 100-μm thick vibratome section. (**J**) Single SBEMR block-face image at the starting point of the reconstruction. The chiasmal, vitreous, central, and scleral surfaces of the reconstruction are identified in **I** and **J**. See Figure 2H for the definition of the FoBMO 30° sectoral acronyms. See Table 1 for acronym definitions.

been performed within the same, peripheral-most, neural canal subregion of the sampled FoBMO sector. Figures 1 to 4 are dedicated to explaining how this has been accomplished. The findings of this study thus pertain only to the peripheral-most axon bundles of the ONH neural canal.

Finally, in two of the five planned comparisons (C4 and C5; Table 3), axon tracing in the EG eye was not possible (see Methods). Therefore, the primary hypotheses of this study have been tested in $n = 3$ SBEMR comparisons (C1, C2, and C3, from NHPs 1 and 2; Table 2), which sampled EG eye regions of 0% to −20% longitudinally detected, OCT retinal nerve fiber layer thickness (RNFLT) loss and −8.3%, −15.2%, and −32.9% RON axon loss.

Methods

Overview

The Methods section is structured as outlined in Figure 1 with the 10 subsections from that figure in bold text below followed by "Reproducibility" and "Statistical Analysis" sections. Table 1 provides a list of the acronyms used in this report and their definitions.

Animal-Unilateral EG Euthanasia Post-mortem Tissue Processing. All animals were treated in accordance with the ARVO statement for the use of animals in research and were approved by the Legacy Institutional Animal Care and Use Committee (IACUC) (Protocols 07–09 and 10-07) (Fig. 1, sections 1, 2, and 3). These protocols are authorized by USDA license (92-R-0002) and are governed by an assurance with the Office of Laboratory Animal Welfare (A3234-01) as well as Legacy Policy (100.16). The Legacy Department of Comparative Medicine supervises all aspects of animal care and maintains full the association for assessment and accreditation of laboratory animal care (AAALAC) accreditation (Unit#000992). Three NHP rhesus macaques (*Macaca mulatta*) were housed in a temperature- and humidity-controlled room with a 12-hour light/12-hour dark cycle and provided with food and water ad libitum. Animal demographics are shown in Table 2.

Our NHP EG model has previously been described.[8,46] For this study, early EG was defined to be the onset of ONH surface change as revealed by longitudinal confocal scanning laser tomography (Heidelberg Retinal Tomography [HRT]; Heidelberg Engineering, Heidelberg, Germany) acquired (along with measurements of IOP) during standard imaging sessions performed at baseline (three to five indi-

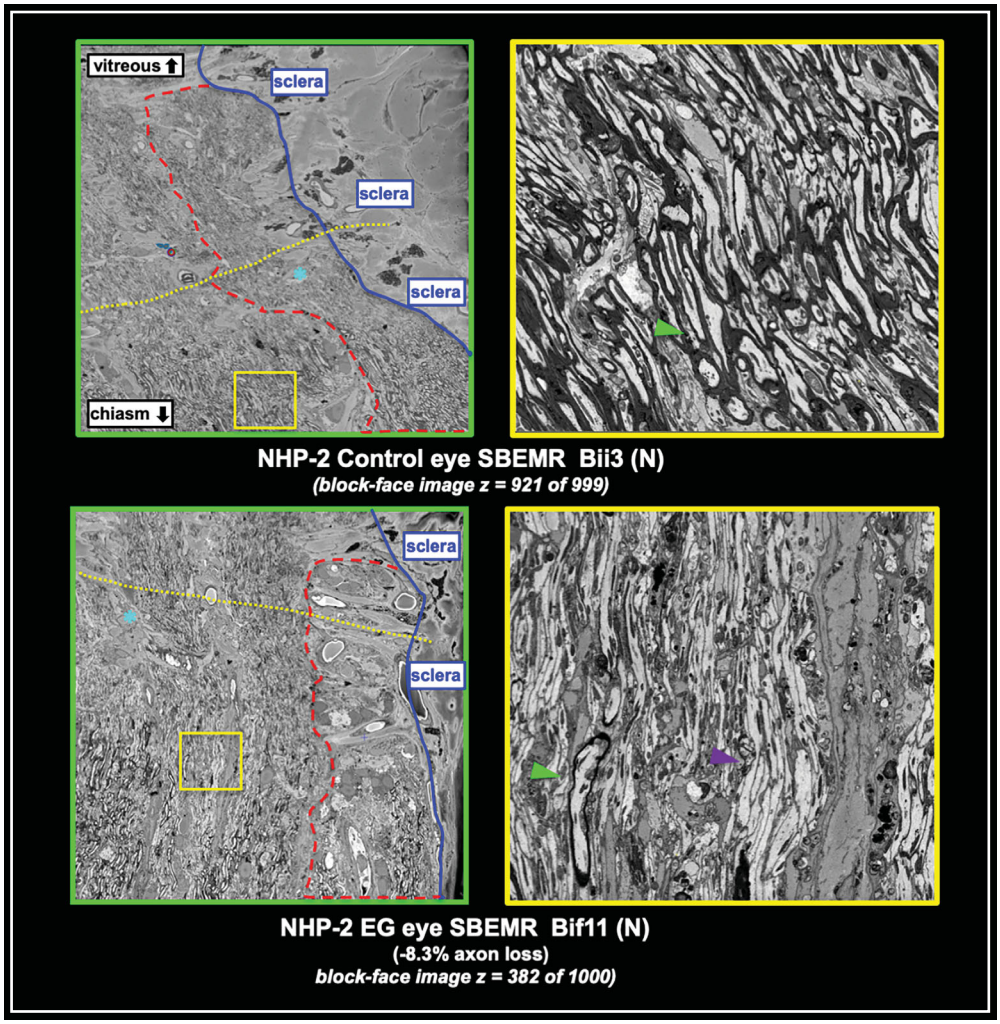

Figure 4. Representative SBEMR block-face images from the control eye (*top*) versus EG eye (*bottom*) SBEMRs that constitute SBEMR comparison 2 (Table 2). Note that for presentation purposes, every SBEMR, regardless of its FoBMO sectoral location within the ONH (Fig. 2), is presented in the same orientation (vitreous up, chiasm down, sclera and peripheral-most axon bundles to the right). Each SBEMR thus samples the peripheral-most axon bundles, the laminar insertion zone of the perineural canal sclera, a portion of the peripheral lamina cribrosa (portions of the laminar beams are present but their transverse connectivity is not apparent in individual SBEMR section images), and the immediate RON. Both the control eye SBEMR ("Bii3") (*top*) and the EG eye SBEMR ("Bif11") (*bottom*) are from the nasal (N) ONH FoBMO 30° sector (Fig. 2H). Both SBEMRs are 200 × 200 × 50 microns in size (see Table 2 and Methods). The block-face images shown here are in the middle of each SBEMR (note the z-axis location of each). Note that in the control eye SBEMR (*top*), myelin does not start immediately behind the 4XμCTR transposed PLS. However, an expanded retrolaminar region of absent and/or disrupted myelin is qualitatively present in the EG eye SBEMR (*bottom left* and *right*). The *yellow dotted line* represents the transposed PLS. The *red dashed line* outlines the most peripheral axon bundle. *Dark blue* outlines the sclera. The *blue asterisks* in the *left* images mark the unmyelinated region of retrolaminar axons in the control (*top*) and EG (*bottom*) eye. Note that there are virtually no myelinated axons through the full extent of the retrolaminar peripheral axon bundle in the EG eye SBEMR (*bottom*). Higher-magnification views (*right*) are taken from locations in the *left* images (*yellow boxes*) that are at similar distances behind the PLS. *Green arrowheads* on the *right* show representative myelinated axons that are virtually absent in the EG eye SBEMR (*bottom right*). See Figure 2 for an explanation of how we estimate the magnitude of EG eye axon loss and disruption (by count, shape, and density) (Table 2), within the FoBMO ONH sector sampled by a given SBEMR comparison. See Figure 5 for an introduction to the x-, y-, and z-axes of each SBEMR and an explanation of our method for tracing structurally intact axons through the SBEMR and identifying their myelin onset point for the purpose of MOD measurement. See Figures 6 to 8 for an explanation of our method for generating the PLS within the 4XμCTR of the vibratome section and its transposition to the SBEMR (*yellow dotted lines above*). See Figure 9 for an explanation of the SBEMR MOD calculation itself. See Table 1 for acronym definitions where not defined herein.

vidual sessions prior to laser) and every 1 to 2 weeks post-laser (i.e., following the onset of unilateral Argon laser to the trabecular meshwork to induce moderate experimental IOP elevation). Our definition of HRT-detected ONH surface change required confirmation from two subsequent imaging sessions. Longitudinal OCT measurements of RNFLT (standard 3.5-mm circle scan) were also performed but not used in defining EG onset.

IOP was measured at the start of each imaging or laser session by Tonopen XL (Reichert, Inc., Depew, NY, USA) in both eyes of each animal (mean of $n = 3$ measures per eye) following an induction dose of ketamine (15 mg/kg intramuscular [IM]) and either xylazine (0.8–1.5 mg/kg IM) or midazolam (0.2 mg/kg IM). All animals were euthanized by pressurized (25 to 35 mm Hg) 2% paraformaldehyde and 2.5% glutaraldehyde perfusion fixa-

tion (made fresh a day before perfusion, kept at 4°C) delivered via a catheter into the left ventricle of the heart under deep isoflurane anesthesia. Eyes were enucleated immediately following perfusion fixation, opened posterior to the limbus, and placed into 2% paraformaldehyde and 2.5% glutaraldehyde overnight for next-day processing.

For each eye, orbital tissues were removed to bare sclera (Fig. 2A), and the dural sheath was carefully dissected away from the orbital optic nerve. The fovea was projected to the posterior scleral surface by passing a suture through the foveola (Fig. 2A). The foveola was visually projected to the temporal midline of the orbital optic nerve at its insertion into the globe and then projected along the length of the orbital nerve by making a shallow cut (Fig. 2A). Two superior cuts along the nerve were then added for further orientation. The orbital optic nerve was then severed with a razor blade 3 mm posterior to the globe for later serial 100-µm vibratome sectioning and axon count analysis (Figs. 2B, 2C, 2D; see next section).

The ONH tissues were then trephined out of the posterior ocular shell using a (10-mm) (Figs. 3A, 3B) trephine (circular blade). For each eye, the OCT-defined FoBMO axis (Fig. 3A) axis (an estimate of the anatomic retinal temporal raphe) was used as a guide to cut the trephine into superior and inferior hemi-trephines for later serial 100-µm vibratome sectioning (Figs. 3B–D).

Estimating EG Versus Control Eye Optic Nerve Axon Loss by 30° FoBMO Sectors for Each SBEMR Comparison. For each eye, the orbital optic nerve was cut into serial 500-µm vibratome sections that were ordered from proximal (abutting the ONH trephine optic nerve stump) to distal (progressively further away from the stump toward the chiasmal end of the tissue piece) (Fig. 1, section 2 and Fig. 2). The most proximal vibratome section was embedded in plastic and serial 1-µm-thick sections were stained and imaged at high resolution (Fig. 2C). To reduce the effects of variable size and shape among axon count section images, the centroid of each axon within the axon count image was "cylinderized" into a standard circle.[47] Estimated 30° FoBMO sectors were projected onto each cylinderized axon count section image by colocalizing it to the orbital optic nerve stump-face image using the temporal and superior cuts common to each nerve stump and axon count section image (Figs. 2B, 2C). Each axon was automatically identified using custom software[47] and the number, size, and density of axons were calculated for each FoBMO sector and then within the most peripheral, mid-peripheral, and central portions of each sector (Fig. 3, lower middle panel).

Generating Serial, FoBMO-Parallel, 100-µm-Thick ONH Trephine Vibratome Sections From Each Eye, Estimating Their FoBMO Clinical Location, Choosing Candidate Vibratome Sections Based on FoBMO Sectoral Axon Loss, and 4× Micro–Computed Tomography Reconstruction of Each Candidate Section. The superior and inferior ONH hemi-trephine tissues were separately embedded and serial 100-µm vibratome sectioned approximately parallel to the FoBMO axis (Figs. 3A–D) (Fig. 1, section 3 and Fig. 3). To choose EG and control eye sections from the same 30° FoBMO sector in both the EG and control eye (i.e., to

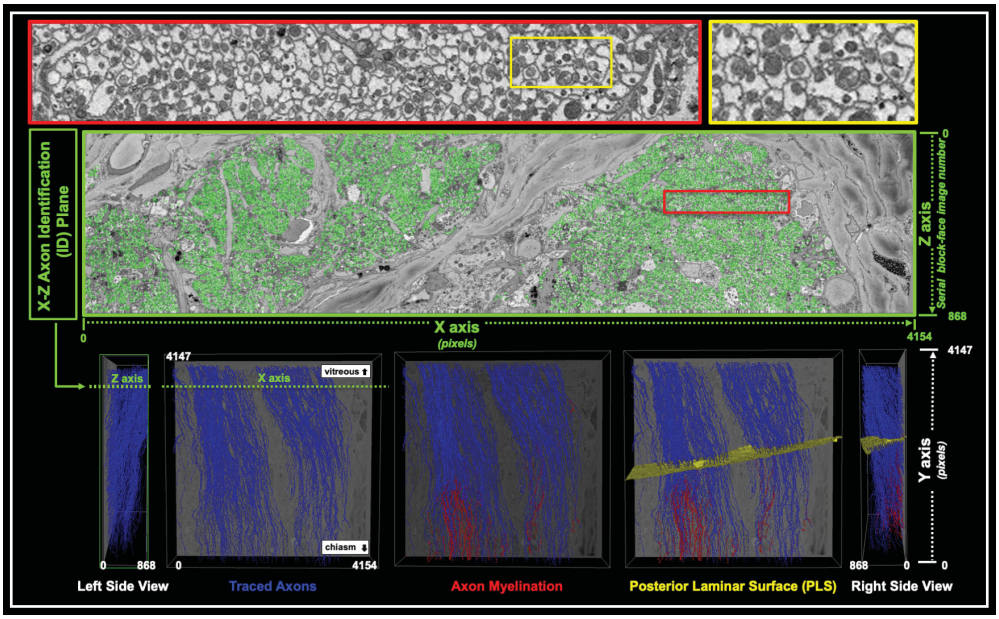

Figure 5. Traced, structurally intact axons (*blue*) within a representative SBEMR (NHP2-EG-Big4 [TI]) with myelin (*red*) where present relative to the SBEMR PLS. *Top*: Higher-magnification views are shown of the axons within the *red rectangle* in the *middle*. *Middle*: All axons within an x–z axon identification plane (located within the lamina) were digitally identified, and then a subset of 300 axons was randomly chosen (in a manner intended to achieve an equal distribution throughout the x and z extent of the identification plane) for tracing. *Bottom*: From the subset of 300 targeted axons, each randomly selected axon was 3D traced through its full extent until it either ended within the block (nonintact) or left the block (intact). For each intact axon, the myelination onset point was marked, when present. Intact axons without myelin were labeled "unmyelinated." Individual axons were traced within each SBEMR until approximately 50 structurally intact myelin onset axons were identified. All axon tracing was done without operator awareness of the position of the PLS within the SBEMR. The "Traced Axon," "Axon Myelination," and "Posterior Laminar Surface" panels are a view of the traced axons through the "front" of the SBEMR shown against the z = 1 (bottom of the SBEMR) block-face image for context. The "Left Side View" (*far left*) shows the traced axons (without PLS) from the left side of the SBEMR. The "Right Side View" (*far right*) shows the traced axons and the PLS (*yellow*) from the right side of the SBEMR. See Figure 9 for additional details. See Table 1 for undefined acronym definitions.

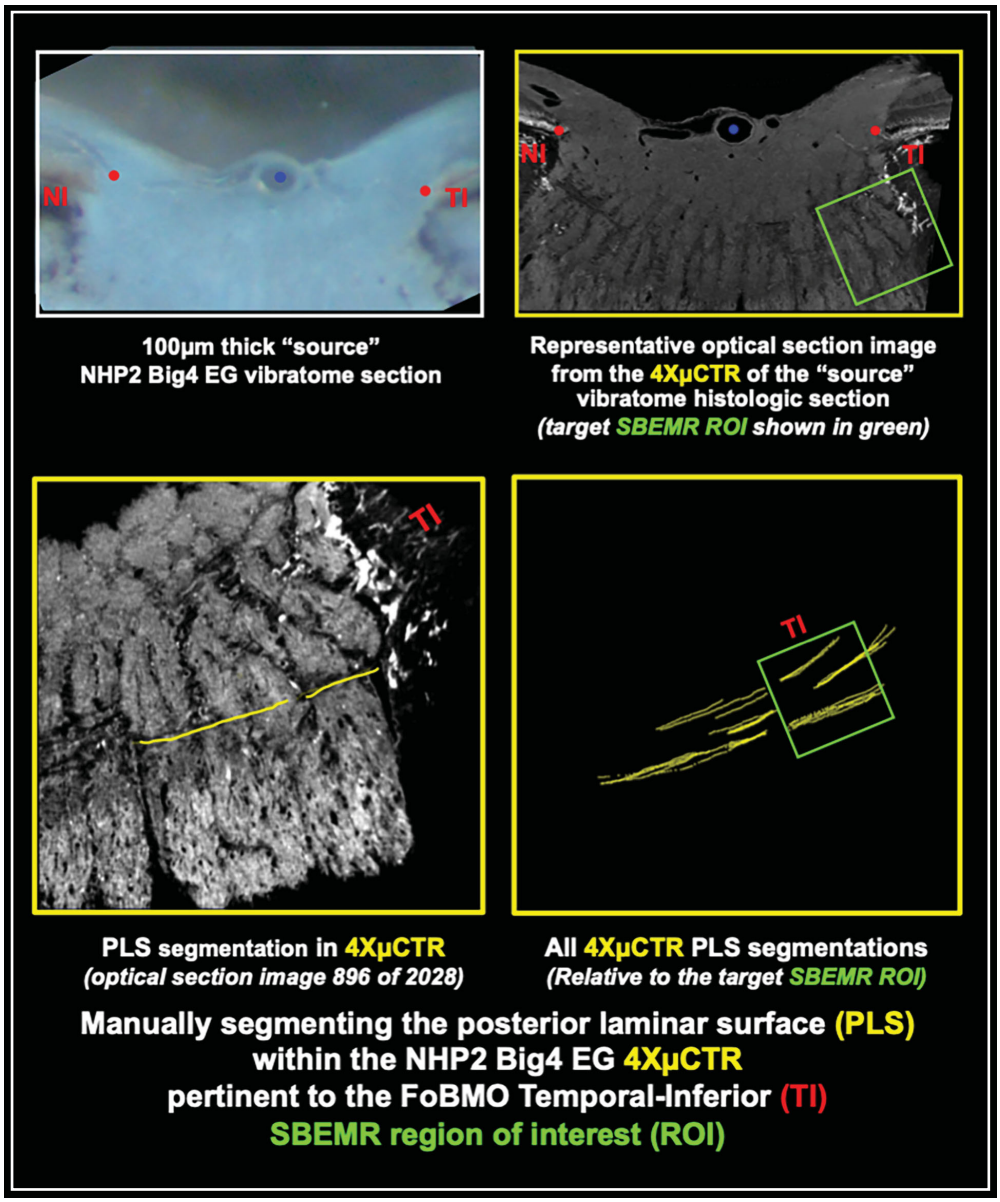

Figure 6. Manually segmenting the PLS (*yellow*) within the 4XµCTR of the NHP2 Big4 EG eye source vibratome section from comparison C3. *Upper left*: Source NHP2 Big4 EG eye vibratome section. *Upper right*: A representative optical section image from the 4XµCTR of the Big4 vibratome section with the target "TI" location of the Big4 SBEMR noted by the *open green square*. *Lower left*: PLS segmentation within another representative optical section image from the 4XµCTR. *Lower right*: All 4XµCTR PLS segmentations in 3D space (as viewed from the "top" of the 4XµCTR), relative to the planned region of the Big4 SBEMR (*green box*). A surface is fit to these segmentations and then transposed into the Big4 SBEMR, as shown in Figures 7 and 8.

create an anatomically consistent control for the EG eye section), the FoBMO location of each EG and control eye vibratome section was estimated on an ONH color photo of the sectioned eye (Figs. 3D–G), as previously reported by Chaudhary et al.[46] Using a line connecting the two BMO points as a reference, the location of the center of each vessel was projected to this BMO reference line. This line, along with its vessel projection points, was then overlaid on a fundus image and affine transformed,[47,48] until the position of best fit for both the BMO points (to the clinical disc margin) and central vessel points (to retinal and optic disc vessels). The orientation of each individual section was then approximated relative to the cardinal sections by using the section number and fine-tuned using the vessel crossings and BMO points as outlined above.

For each SBEMR comparison, the selected EG and control eye "source" vibratome sections were treated with heavy metals and embed in resin.[49,50] For each (now optically opaque) section, the entire section was imaged by micro–computed tomography (µCT) at 4× magnification (4XµCT) using a Versa 510 X-ray microscope (Zeiss) to determine the target SBEMR region of interest (ROI).[49] Because, for this study, the target anatomy for each SBEMR was the peripheral-most neural canal (laminar) and RON axon bundles, the target ROI for each SBEMR included a thin portion of the juxta-canalicular sclera and pial sheath

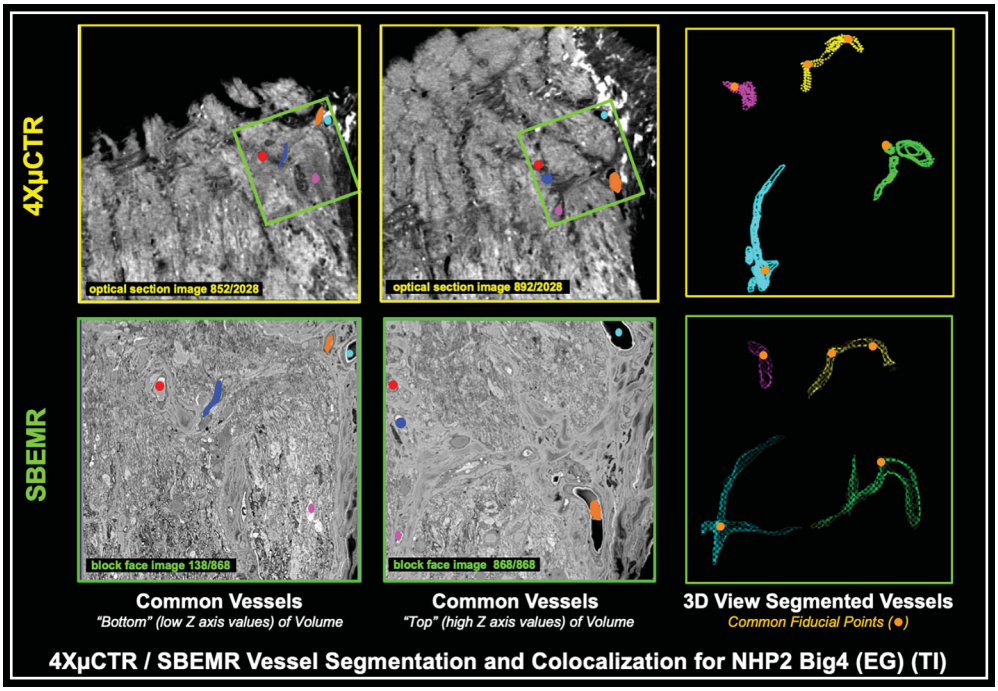

Figure 7. The 4XμCTR/SBEMR vessel identification, segmentation, fiducial point selection, and volume colocalization. *Left and middle*: Vessels that are common to both the 4XμCTR (*upper*) and SBEMR (*lower*) volumes are identified first at the "bottom" (z = low values, *left*) and "top" (z = high values, *right*) of the 4XμCTR optical section images (*upper*) and SBEMR block face images (*lower*) (see Fig. 6). Vessels that can be identified in both volumes are then traced through their full extent in both the 4XμCTR and SBEMR volumes. *Right*: Segmented vessels from both the 4XμCTR (*upper*) and SBEMR (*lower*) volumes are viewed simultaneously to identify common branch points that can be used as fiducial points for colocalization (see Methods).

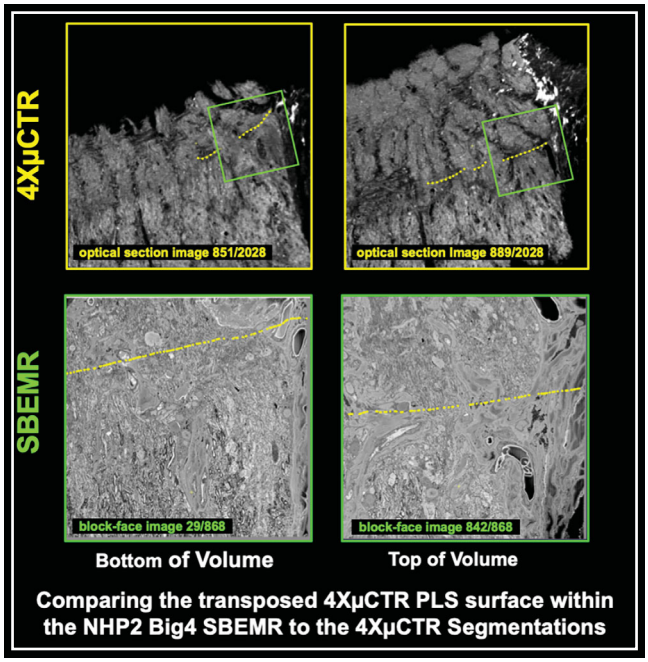

Figure 8. Comparing the manual PLS segmentations within the "bottom" (*left*) and "top" (*right*) optical section images of the 4XμCTR (*above*) to the SBEMR (*below*) volumes. The 4XμCT PLS segmentations in the top row are the manual segmentations made within the block-face images of the 4XμCT volume. The PLS segmentations within the SBEMR block-face images on the bottom are facet point depictions of the 4XμCTR fitted PLS surface after it has been colocalized into the SBEMR using the fiducial points shown in Figure 7. Close inspection of the PLS surface at both the top and bottom locations of each volume demonstrates the PLS position to be similar relative to laminar, vascular, and scleral anatomic landmarks common to both volumes.

as "peripheral" neural canal landmarks (Figs. 3E, 3I, 3J and Fig. 4).The section was then roughly trimmed and mounted on an Aclar sheet, glued to the top of a mounting cylinder (Ted Pella, Redding, CA, USA), and reimaged at higher resolution (20×) μCT, to finalize the optimal z-axis location and extent of the SBEMR within the thickness of the section. Precise trimming of the specimen ROI was followed by ultramicrotome removal of excess resin from the bottom of the sample to optimally expose the tissue for SBEM imaging.

Generating EG/Control Eye SBEMRs From the Target ROI of Their Respective Vibratome Sections. For each SBEMR, the final vibratome section specimen block (~1 × 1 mm) was mounted to the top of an SBEM sample pin using conductive resin (Ted Pella) (Fig. 1, sections 4 and 5; Figs. 3I, 3J; and Fig. 4). Sample trimming was completed using an ultramicrotome. SBEM imaging after serial removal of the block face in 50-nm increments was performed using a Sigma SEM (Zeiss) equipped with a 3View 2XP stage (Gatan, Pleasanton, CA, USA) at 2.0 Kilo electron volt. The serial block-face images for each SBEMR were aligned by cross-correlation using IMOD 3D visualization software (http://bio3d.colorado.edu/imod/) to produce final SBEMRs (i.e., aligned three-dimensional volumes) (Figs. 3 and 4). After 5 × 5 transverse pixel binning to reduce computer memory demand, each SBEMR was imported into IMOD for axonal tracing and myelin onset distance (MOD) analyses (Fig. 5).[51] Details regarding the x-y-z volume extent, as well as the acquired and IMOD analysis pixel and voxel size within each study SBEMR, are reported in Table 3.

Manually Tracing Axons Within Each SBEMR and Determining Their Myelin Onset Point. Using IMOD, all axons were manually identified within a single digital "x–z" section image (Fig. 5) that was positioned within

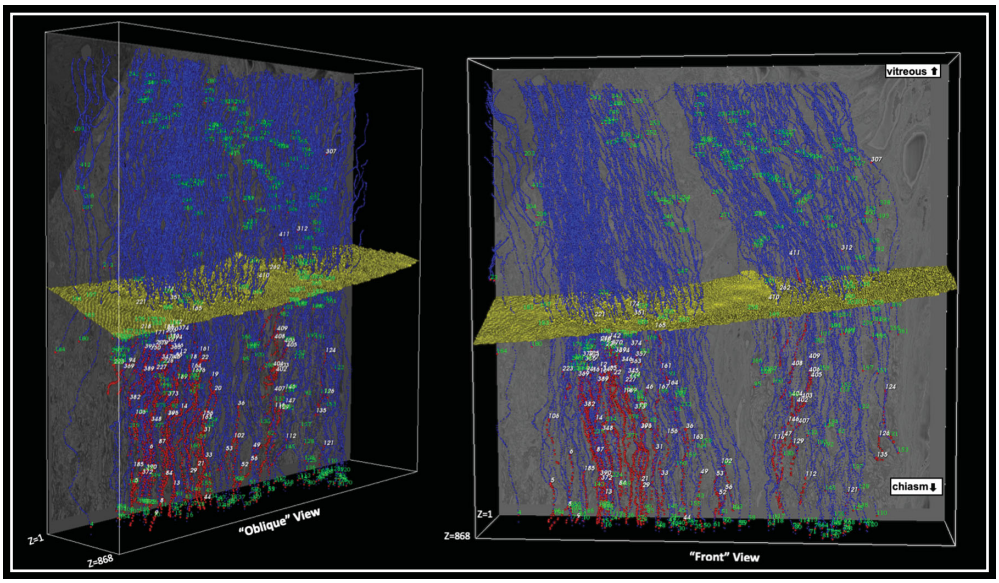

Figure 9. MOD calculations relative to the transposed 4XμCTR PLS within the NHP2 Big4 EG (TI) SBEMR shown in Figure 5. *Blue* denotes the unmyelinated portion of each traced axon. *Red* denotes the myelinated portion of each traced axon where present. *Yellow* denotes the transposed 4XμCTR PLS (see Figs. 7 and 8). *White numbers* denote traced axons that are myelinated within the SBEMR. *Green numbers* denote traced axons that exit the SBEMR without myelin. For each traced axon that crosses the PLS, if a myelin onset point is identified, MOD is defined to be the linear distance along the traced axon "spline" from its intersection with the PLS. For those axons with a myelin onset point "below" (i.e., "chiasmal to") the PLS, the MOD value is defined to be (+) in sign. For those axons with a myelin onset point "above" (i.e., "vitreal to") the PLS, the MOD value is defined to be (–) in sign. For each traced axon that crosses the PLS and exits the block without the identifiable onset of myelin, the MOD is estimated (for "survival" analysis purposes) by the linear distance along the traced axon from its exit point to the PLS. Traced axons that exit the block above the PLS are not included in the analysis.

the laminar tissues parallel to the vitreous surface of the SBEMR (Fig. 1, section 6 and Fig. 5). From these axons, a subset of 300 randomly distributed axons were identified (targeted) and ordered for manual segmentation so as to achieve an equal distribution of traced axons throughout the x and z extent of the identification plane. From

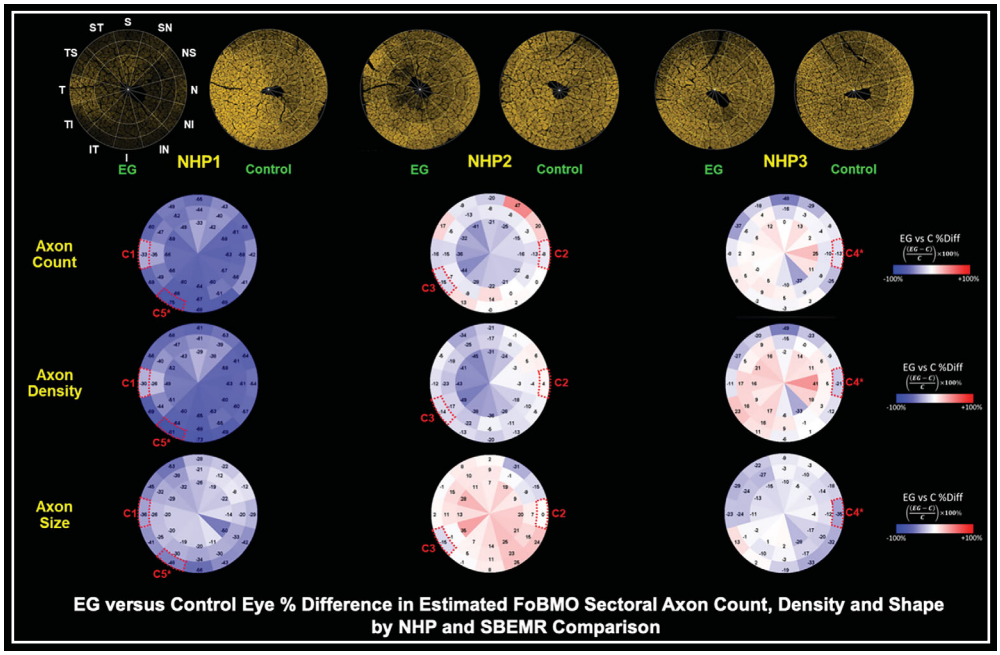

Figure 10. EG versus control eye percent difference in estimated FoBMO sectoral axon count, density, and shape by NHP and SBEMR comparison. *Upper row*: Cylinderized EG and control eye orbital optic nerve image for each studied NHP. Middle-upper, middle-lower, and lower row images are EG versus control percent difference maps for axon counts, axon density, and axon size (respectively) for each NHP. Data for the peripheral, middle, and central subregions of each FoBMO sector are shown. All SBEMRs sampled the peripheral most subregion of a given FoBMO sector. The location of the five EG versus control eye SBEMR comparisons (C1, C2, C3, C4*, and C5*, in *red*) are shown within the specific FoBMO sector of the NHP in which that comparison was performed (see Table 2). For comparisons C4* and C5*, only control eye data were available (see Methods). See Figure 2 for the definition of the FoBMO sectoral acronyms in the *upper row left*.

this subset of targeted axons, individual axons were three-dimensionally traced through the SBEMR for their full extent until either they ended within the block (nonintact) or left the block (intact). For each intact axon, the myelination onset point, when present, was marked. Intact axons without myelin were labeled "unmyelinated." Individual axons were traced within each SBEMR, until approximately 50 structurally intact, myelin onset axons were identified (Fig. 5).

In the case of two EG versus control eye SBEMR comparisons (comparisons C4 and C5; Table 3), axon tracing was not possible within the EG eye SBEMR. In the case of comparison C4, serial block-face image acquisition was inadvertently disrupted, creating a large gap within the center of the SBEMR, across which axon tracing was not possible. In the case of comparison C5, while the overall goal of this report was to study early to moderate EG, we included this region to sample a more severely damaged eye for learning purposes and context. However, upon completion of the SBEMR, axonal disruption was so profound that axon tracing was not possible. Because the control eye SBEMRs from each comparison were of excellent quality, axons were traced within both control eye SBEMRs and included in experiment-wide EG versus control eyes comparisons (see Results).

Segmenting and Surfacing the PLS Within the EG and Control Eye 4XμCTR ROI of Each SBEMR Comparison. We have previously defined the PLS within three-dimensional (3D) histomorphometric ONH reconstructions based upon the transverse (i.e., parallel to the sclera) orientation and connectivity of the laminar beams relative to the more "axial" or "longitudinal" orientation of the retrolaminar connective tissue septa of the orbital optic nerve (Fig. 1, section 7 and Fig. 6).[9–12,15] However, because the z-axis thickness of each SBEMR was only 50 or 75 μm (Table 3), the number of transversely connected laminar beams within an individual SBEMR was limited, and PLS segmentation using this approach was highly variable among operators. We therefore segmented and surfaced the posterior-most laminar beams within the 4XμCTR of its source vibratome tissue section because the 100-μm thickness of the section increased the number of identifiable posterior laminar beams, making the method more reproducible (see below).

For each SBEMR, the posterior surface of the posterior-most laminar beams was segmented within the 4XμCTR of the source vibratome section using IMOD software (Fig. 6). For this step, transversely oriented posterior laminar beams were distinguished from the more longitudinally oriented retrolaminar septa, by requiring them to be continuously, transversely connected to adjacent beams as previously described (above).[52,53] Within each 4XμCTR, PLS segmentation was performed both within and beyond the SBEMR ROI (Fig. 6, lower right) so as to improve the reproducibility of the final position of the 4XμCT PLS within the SBEMR after colocalized transformation (as explained in Figs. 7 and 8). A best-fit 4XμCTR PLS surface was achieved using the 4XμCTR PLS segmentation points exported from the IMOD PLS segmentation model and custom software incorporating the visualization toolkit (VTK). The PLS surface was saved as an STL file (StereoLithography file format) and as a separate model consisting of the surface facet points, which allowed visualization of the surface (post-colocalized transformation from the 4XμCTR) within the SBEMR (Figs. 8 and 9).

Segmenting Common Vessels Within the EG and Control Eye 4XμCT/SBEMR Digital Volume Pairs of Each SBEMR Comparison to Identify Common Colocalization Fiducial Points in Each Volume. Vessels common to both the 4XμCTR and SBEMR volumes were identified first at the "bottom" (z = low values) and "top" (z = high values) of each volume and then traced through their full extent in both the 4XμCTR and SBEMR (Fig. 1, section 8 and Fig. 7). Segmented vessels from both volumes were then viewed simultaneously within IMOD to identify common branch points, which could then be used as fiducial points for colocalization (Fig. 7).

Colocalizing the Paired 4XμCT and SBEMR Volumes of Each Eye Using Their Common Segmented Vessels to "Capture" the 4XμCTR PLS Surface Within the SBEMR. Using the identified common fiducial points (Fig. 7), the smaller SBEMR was 3D colocalized into the source 4XμCTR volume using a "closest point algorithm," allowing the 4XμCTR PLS surface to be transferred into the SBEM as "facet points" from which an SBEMR PLS surface was generated (Fig. 8), (Fig. 1, section 9 and Fig. 8).

Measuring the MOD of Each Traced Axon Within the EG and Control Eye SBEMRs Relative to the SBEMR PLS. Within each SBEMR, for each traced axon that crossed the PLS, if a myelin onset point was identified, MOD was defined to be the linear distance along the traced axon "spline" from its intersection with the PLS (Fig. 1, section 10 and Fig. 9). For those axons with a myelin onset point "below" (i.e., "chiasmal to") the PLS, the MOD value was defined to be (+) in sign. For those axons with a myelin onset point "above" (i.e., "vitreal to") the PLS, the MOD value was defined to be (–) in sign. For each traced axon that crossed the PLS and exited the block without the identifiable onset of myelin, the MOD was estimated, for "survival" analysis purposes, by the linear distance along the traced axon from its exit point to the PLS. Traced axons that exited the block above the PLS were not included in the analysis.

Reproducibility of 4XμCT PLS Segmentation, Surfacing, and Transposition Into the SBEMR for Both the Control and EG Eye SBEMRs of Comparison 3

Among all constituent steps of our method (Fig. 1), we chose to assess the reproducibility of the 4XμCTR PLS segmentation and SBEMR PLS transposition steps because we felt they were the most challenging. To do so, we selected SBEMR comparison (C3) for replication because it demonstrated the smallest magnitude of EG versus control eye MOD difference in the "Original" analysis (see the Results section). We then performed two independent replications of the PLS segmentation, surfacing and transposition steps (reproducibility 1 [Repro1] and reproducibility 2 [Repro2]), more than 6 months after the "Original" analysis and separated the replications by 1 month. Both the Repro1 and Repro2 analyses were performed by the same operators who did the "Original" PLS and vessel segmentations (CFB) as well as the "original" PLS surfacing, fiducial point selection, and 4XμCT to SBEMR transposition (HL). For both the Repro1 and Repro2 analyses, both operators were completely masked to their previous work. The ability to detect EG versus control eye MOD differences in the Repro1 and Repro2 versions of the MOD was then assessed by survival analysis.

Table 4. Numbers of Traced Axons, Myelin Onset Axons, and Unmyelinated Axons Within the Control and EG Eye SBMERs of Each Comparison

EG vs. C SBEMR Comparison Number*	NHP Study ID	EG Eye SBEMR ID†	EG Eye: Number of Traced Axons	EG Eye: Number of Myelin Onset Axons	EG Eye: Number of Unmyelinated Axons	Control Eye: SBEMR ID†	Control Eye: Number of Traced Axons	Control Eye: Number of Myelin Onset Axons	Control Eye: Number of Unmyelinated Axons
C1	NHP1	Bhx8	86	58	28	Bhz2	105	89	16
C2	NHP2	Bif11	206	88	118	Bii3	142	64	78
C3	NHP2	Big4	293	90	203	Bii5	351	83	268
C4	NHP3	Not available‡				Bin11§	61	48	13
C5	NHP1	Not available‖				Bia8§	167	126	41

We report a total of $n = 3$ EG versus control eye SBEMR comparisons. In two additional comparisons, axon tracing in the EG eye was not possible (see Methods), but for both comparisons, control eye SBEM data were used in a subset of analyses (see Methods). For details on SBEMR volume and voxel size, see Table 3. $n = 5$ EG versus control eye SBEMR comparisons were planned; for comparisons 4 and 5, EG eye data were not available (see table and Methods).

* Each EG versus control eye SBEMR comparison used tissue from the same 30° ONH sector—see Figure 2D and its legend for the FoBMO sectoral identifiers and their names. See Figure 10 for the FoBMO sectoral location of the SBEMRs in each comparison.

† Unique four-digit identifier for each SBEMR.

‡ EG eye data not available because an SBEM gap in acquisition did not allow axon tracing (see Methods).

§ While EG eye data were not available for this comparison, the control eye data were used in a subset of analyses.

‖ EG eye data not available because the extent of damage was beyond early moderate to EG and did not allow axon tracing (see Methods).

Statistical Analyses

For each SBEMR comparison, survival analysis was done in R (version 4.0.3; R Project for Statistical Computing, Vienna, Austria) to compare EG eye MOD to control eye MOD while accounting for the variable numbers of myelin onset axons and unmyelinated axons within the EG and control eye SBEMRs of each comparison by treating axons as being censored at the point at which they exited the section if no myelin onset was detected.[54]

Results

Post-Mortem Estimated FoBMO Sectoral Axon Count Data Suggest That the EG Eye Damage Studied Was Early (<16% Axon Loss) for SBEMR Comparisons 2 and 3 and Moderate (<33%) for Comparison 1

Animal demographics, IOP data, EG versus control eye OCT global RNFL thinning, and global orbital optic nerve (ON) axon loss at the time of euthanasia are reported for each of the three unilateral EG study NHPs in Table 2 (Fig. 10). Similar data for the specific FoBMO sectors studied in each of the three SBEMR comparisons are reported in Table 3. Complete FoBMO sectoral EG versus control eye differences in axon counts, axon size, and axon density measurements are reported in Figure 10.

Global EG eye RNFL thinning compared to baseline was 31.2% in NHP1, 11.1% in NHP2, and 5% in NHP3. Global, EG eye axon loss was 54% in NHP1, 10.9% in NHP2, and 5.5% in NHP3.[55,56] Figure 10 reports FoBMO sectoral axon count, axon density, and axon size data for all three NHPs, with the animal and FoBMO sectoral location for each SBEMR comparison superimposed on the data plots.

Structurally Intact Axons in the EG Eyes of All Three SBEMR Comparisons Demonstrate Increased Myelin Onset Distance From the PLS by Survival Analysis

The numbers of traced axons, myelin onset axons, and unmyelinated axons within the control and EG eye SBMERs of each comparison are reported in Table 4 (Figs. 11 and 12). For all three SBEMR comparisons, the proportion of unmyelinated axons at each retrolaminar distance was significantly increased in the EG compared to the control eye SBEMR ($P < 0.001$, Fig. 11). Median MODs for the control versus EG SBEMRs of each comparison were 19.8 vs. 119.9 µm for comparison C1, 94.0 vs. 187.4 µm for comparison C2, and 78.4 vs. 147.8 µm for comparison C3, respectively. When data from all three EG eye SBEMRs were pooled and compared to data from all five control eye SBEMRs, the proportion of unmyelinated axons at all retrolaminar distances remained significantly increased within the pooled EG eyes (Fig. 12).

Statistically Significant EG Versus Control Eye MOD Differences Were Present in the "Repro1" and "Repro2" Versions of the Reproducibility Study

While there were qualitative differences in the "tilt" of the PLS among the "Original," "Repro1," and "Repro2" versions

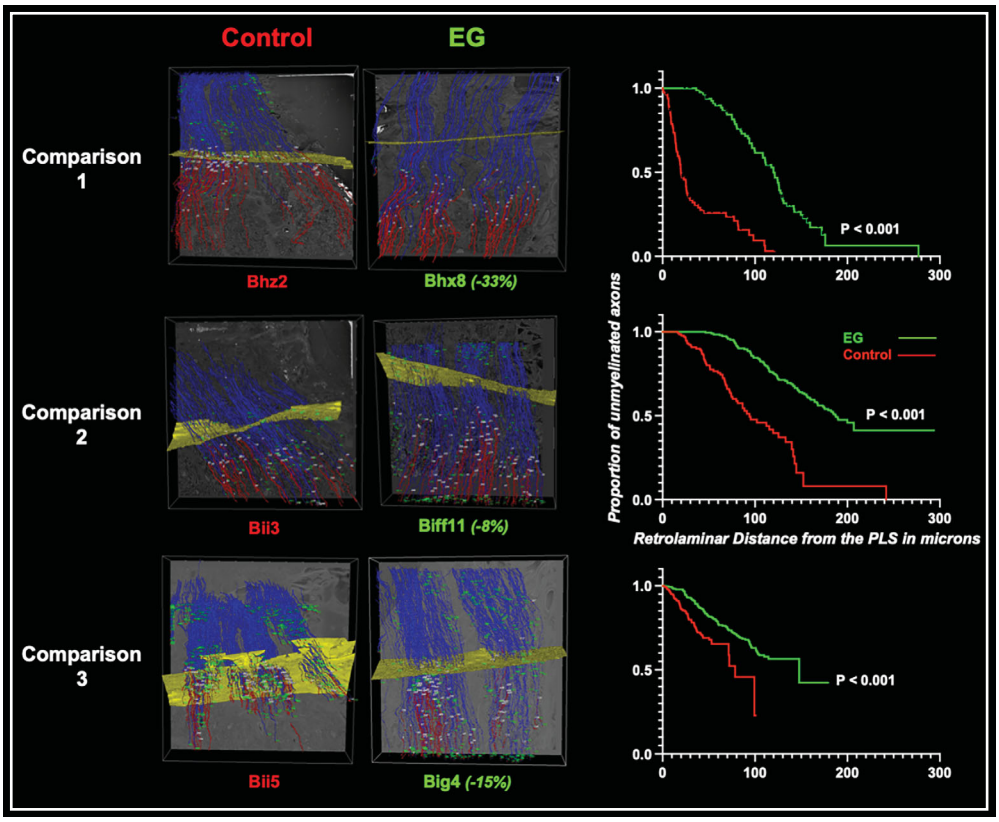

Figure 11. MOD measurements and survival curves for the three EG versus control eye SBEMR comparisons of this study. See Figures 3 to 5 for detailed explanation of the colored components and orientation of each SBEMR. The number in parentheses after each EG eye SBEMR four-digit identifier is the percent EG versus control eye axon count difference for the sampled sector (see Table 2). Details for each survival curve are shown for comparison 2 (*middle right*). While the proportion of unmyelinated axons at each retrolaminar myelin distance is significantly higher for the EG (*green*) versus its control (*red*) eye SBEMR for all three comparisons, the magnitude of the difference is smallest for comparison 3 (NHP2 Big4 EG versus Bii5 control). As such, the reproducibility study used the two comparison 3 SBEMRs to assess the ability to consistently detect a significant MOD increase within the EG versus control eye SBEMR, using independent versions of each method step (see Methods and Fig. 13).

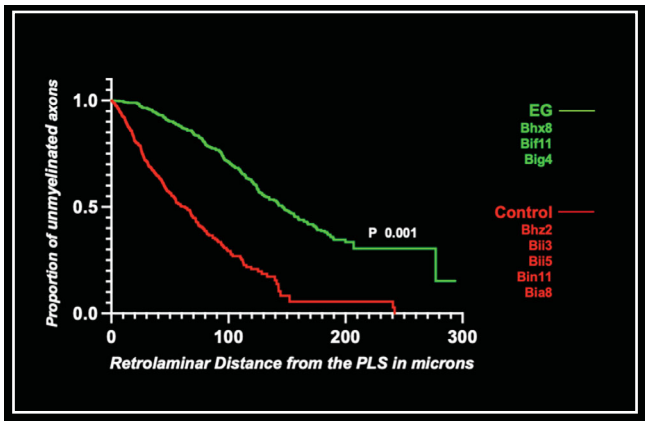

Figure 12. MOD experiment-wide survival curves for the pooled ($n = 3$) EG eye (*green*) SBEMRs versus the pooled ($n = 5$) control eye (*red*) SBEMRs.

of the EG and control eye SBEMR PLS(s) (Fig. 13), this did not prevent the detection of increased MOD in the EG versus control eye SBEMRs of the "Repro1" and "Repro2" versions of the MOD data (Fig. 13).

Discussion

We recently employed anatomically consistent techniques to demonstrate retrolaminar myelin-related protein intensity decreases and Iba1-positive and NucBlue pixel-cluster density increases in early to moderate NHP EG by qIHC.[46] The animals in our qIHC study were euthanized at levels of EG eye, RNFL thinning that would not likely be associated with detectable visual field changes in NHPs or humans.[57,58] In that study,[46] RON axon counts were not available for the NHP EG and control eyes.

The SBEMR EG eye findings from the present report are from a separate group of SBEMR-dedicated NHPs, in which all three EG eye FoBMO regions studied demonstrated ≤20% OCT-detected RNFLT loss and RON axon loss of −8.3%, −15.2%, and −32.9%, respectively. Our SBEMR data thus suggest that RON myelin alterations occurred in the setting of early RGC axon loss in NHP EG and provide strong evidence that at this stage of damage, there were also RGC axons that were demyelinated for some distance behind the lamina but were structurally intact through the region of demyelination (at least through the portion of the axon contained within the SBEMR).

The Radius and Pederson[26] report of partial loss of the myelin sheath surrounding axonal segments behind the

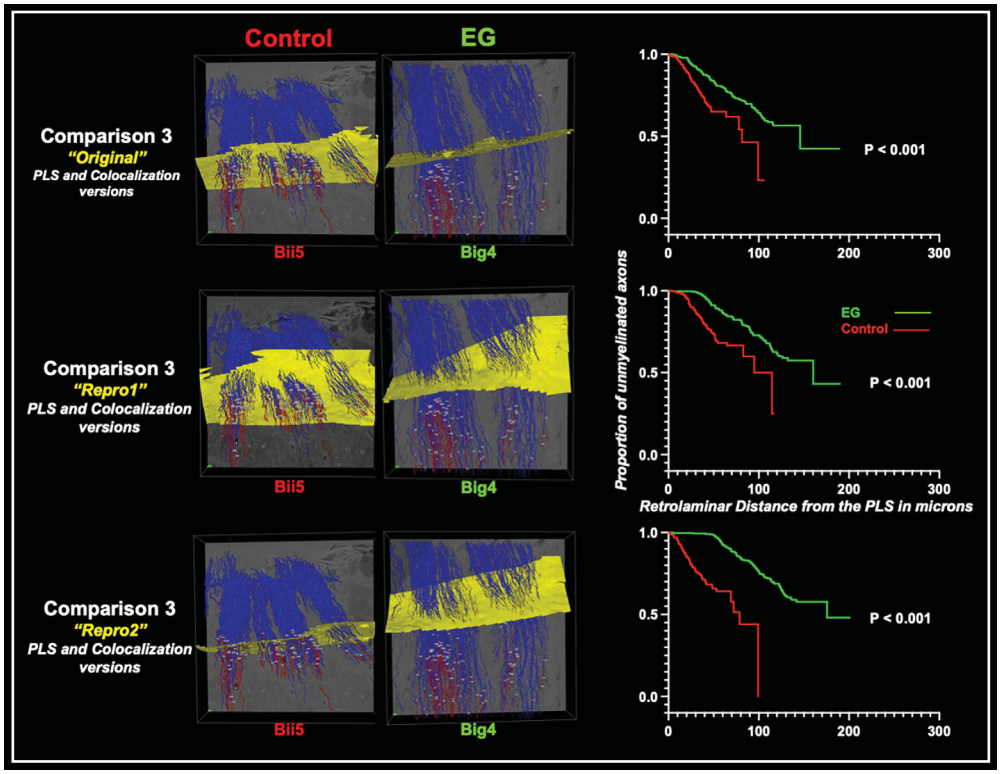

Figure 13. MOD measurements and survival curves for the "Original" (*above*), "Repro1," and "Repro2" versions of both the EG versus control eye SBEMRs of comparison 3. See Figures 3 to 5 for detailed explanations of the colored components and orientation of each SBEMR. See Figure 11 and the Methods section for an explanation of why comparison 3 was chosen for the reproducibility study. An independent (and masked; see Methods) PLS (*yellow*) (Figs. 7 and 8) and 4µCTR/SBEMR colocalization (Figs. 9 and 10) was performed for each of the three study versions (Original, Repro1, and Repro2) by the same operator—separated by at least 1 month. Details for each survival curve are shown for the Repro1 version (*middle right*). While the relative tilt of the PLS varies to some degree within each SBEMR among the three versions, this does not prevent the detection of increased MODs in the Big4 (EG) versus Bii5 (control) eye SBEMRs in the Original. Repro1 and Repro2 versions of the MOD data (*right panels*).

lamina in the NHP unilateral EG model is pertinent to our study. Performed in 1985, using then state-of-the-art methods, EG versus control eye differences in cup/disc ratio and global RON axon count estimates (in which approximately 10% of the axons were manually counted) were used to identify two EG eyes with minimal increases in cup/disc ratio and global RON axon loss of −15% and −36%, respectively. Both EG eyes demonstrated "scattered demyelination of axons" within the "anterior-most part of the retro-orbital (their term for retro-laminar) optic nerve." Transmission electron microscopy (TEM) examination (performed only on tissues from moderate and severally damaged EG eyes) revealed accumulation of cellular debris in axons, which was attributed to focal interruption of anterograde and/or retrograde axonal transport mechanisms as had been previously described by other investigators.[4,5,59–62] No electron microscopic assessment of axonal integrity was reported. However, the authors' use of the term *demyelination* suggests that a disruption of myelin homeostasis may have contributed to the RGC axon alterations they described.

Myelin basic protein and myelin oligodendrocyte glycoprotein messenger RNA expression were decreased in the rat ON after retinal ischemia/reperfusion.[63] Korneva et al.[64] demonstrated that the anterior extent of myelination moved posteriorly in a CD1 mouse–induced glaucoma model. Recent studies suggest that RGC axon myelin homeostasis may be disrupted during development in frogs,[65] as well as within the myelin transition zone in genetic and experimentally induced glaucoma models.[66,67] Smith et al.[45] reported expansion of the node of Ranvier in the DBA2J genetic but not a C57BL/6J-induced glaucoma model at a stage in which anterograde axon transport was absent but retrograde transport was preserved.

Taken together with these previous reports and those of many other investigators, our study contributes to a growing literature that suggests that while RGC axon transport blockade within the ONH tissues is an early event in experimental and human glaucomatous vision loss, there may be a stage of ONH RGC axon homeostasis disruption that coincides with or precedes transport loss and degeneration in which ONH-targeted neuroprotective interventions could be efficacious.[68–70] In these regards, while Smith et al.[45] emphasized node of Ranvier alterations rather than demyelination (although myelin alterations were mentioned) and failed to find these findings in a C57BL/6J EG model (which, like the NHP unilateral EG model, employs induced IOP elevation and lacks the underlying neuroinflammation of the DBA2J model), it is pertinent to the findings of our study for the following reasons. First, the node of Ranvier changes, if looked for in our existing SBEMRs, may also be present at this early stage of the neuropathy. Second, regarding ONH-targeted neuroprotective interventions, Smith et al.[45] also demonstrated that 1 week of systemic treatment with fingolimod (an immunosuppressant therapy for relapsing-

remitting multiple sclerosis) in the DBA/2J mice showed partial reduction in node and axonal pathology. Since we hypothesize that demyelination in NHP early EG centrally involves neuroinflammation,[46] similar or related therapies may be efficacious in NHP-inducible and human glaucoma.

The methods we introduced to achieve anatomically consistent EG versus control eye SBEMR comparisons based on the OCT-determined FoBMO axis have the following implications. First, these strategies will allow FoBMO-consistent central versus peripheral or superior versus inferior versus nasal versus temporal SBEMR comparisons in EG eyes. Second, the relationships between presacrifice, longitudinal EG eye FoBMO sectoral OCT change and post-mortem RON axon counts, qIHC protein expression, TEM, and/or SBEMR EG versus control eye change can be assessed to better understand the cellular mechanisms underlying early OCT change in human ocular hypertension and glaucoma.

Our study has the following limitations. First, the FoBMO 30° sectoral RON axon counts are estimates only, as the foveal projection to the temporal RON is an estimate, the retinal topographic organization of the RGC axons begins to be altered within the ONH neural canal,[71] and the orientation cuts on the RON piece used to generate tissue sections are also estimates. However, acknowledging these issues, we believe our approach is an advance in estimating EG versus control eye retrolaminar axon counts within ONH FoBMO sectors. Future NHP studies using axon transport tracers will allow us to better understand the degree to which retinal topographic organization is maintained within the RON.[71–75] Second, while we emphasize axon counts, we also report size and shape measures as these have strengths and weaknesses as estimates of RGC axon damage. In the future, our goal is to develop "internal" markers of axonal distress based on the morphology of the axons within each SBEMR as well as the presence or absence of preplaced, intravitreal axoplasmic transport markers.[67]

Third, the number of axons traced, as well as the number of structurally intact myelin onset and unmyelinated axons identified in each SBEMR, was limited by the intensive labor requirements of this study. While in general, we randomly traced axons within each SBEMR until at least 50 structurally intact myelin onset axons were identified with the intention of making these axons the primary focus of our analyses, our understanding of the complexity of the "sampling" issues involved in "fairly assessing" retrolaminar myelinization of axons in the EG versus the control eye SBEMRs of each comparison progressively deepened through the five comparisons we assessed.

Fourth, while age is an important risk factor for the development of glaucoma in human eyes and our study NHPs included two young animals (NHP1 and NHP3, age 3) and one old animal (NHP2, age 24), we do not believe that age effects explain our findings for the following reasons. First, our hypotheses were primarily tested within three individual SBEMR comparisons (C1, C2, and C3; Table 2) in which the EG and control eye SBEMRs came from the same NHP, therefore avoiding the effect of animal age. In addition, because the tissues for these three primary comparisons came from NHP1 and NHP2, to include more inter-NHP variability in control eye MOD, we performed a separate experiment-wide comparison between the pooled EG eye SBEMR MOD data of NHP1 and NHP2 and the pooled control eye MOD data from NHP1, NHP2, and NHP3, and we found that even in the setting of increased control eye MOD variability, pooled EG eye SBEMR MOD was greater than pooled control eye SBEMR MOD (Fig. 12). Finally, we tested the hypothesis that MOD was increased in the $n = 2$ old compared to the $n = 3$ young control SBEMRs and found it to be increased in the old control eye SBEMRs with borderline significance (data not shown). Thus, in the experiment-wide analysis, inclusion of the $n = 2$ old control eye MOD data increased control eye SBEMR MOD, making it more difficult to detect a significant experiment-wide increase in the $n = 3$ EG eye SBEMRs. The finding that old control eye MOD is increased compared to young control eyes suggests that retrolaminar myelin homeostasis may be altered in aged NHP eyes. If replicated in follow-up studies that include larger numbers of young and old NHP control (or bilateral normal) eyes, the contribution of myelin homeostasis disruption to age-related glaucoma susceptibility will warrant further study.

Ideally, deep learning axon tracing algorithms that are currently under development will eventually allow us to trace all of the axons within a given SBEMR. Once done, determining those that are intact or nonintact as well as those that have a MOD and those that are unmyelinated will allow the most robust assessment of EG versus control eye SBEMR MOD differences within a given comparison. Within such "total axon" data for a given EG versus control eye SBEMR comparison, a bootstrapping strategy could then be employed to generate thousands of subsampled versions of the EG and control eye axon data. Such an analysis could then be used to identify the subregions of the EG eye SBEMR where the greatest amount of significant MOD difference (by survival analysis) is most consistently detected.

Finally, manual 4×uCTR posterior laminar beam segmentation, PLS generation, and its colocalization into the contained SBEMR all introduce variability in the 3D position of the SBEMR PLS and thus variation in the MOD measurements of each contained axon. However, in a rigorous reproducibility assessment, this variability did not prevent us from consistently detecting increased EG eye MOD in the SBEMR comparison with the smallest EG versus control eye MOD difference. Future deep learning segmentation of the laminar beams and vessels may reduce the variability of this step.

In summary, we used anatomically consistent EG versus control eye SBEMR comparisons to demonstrate that structurally intact axons within the RON of NHP early to moderate EG eyes are demyelinated. Future studies to expand these findings to early axon loss regions of additional SBEMR-dedicated animals, to expand the size of the SBEMRs to encompass longer portions of the axons behind the lamina, to use deep learning axon tracing to study all of the structurally intact axons in a given SBEMR, and to determine the functional status of these demyelinated, structurally intact axons (in new animals) are necessary to confirm the importance of our findings. Studies to determine the mechanisms responsible for demyelination so as to effectively reduce or prevent its occurrence and effects are ongoing. Translational studies to link the post-mortem tissue presence of demyelinated structurally and functionally intact axons to the colocalized, longitudinal OCT tissue signal intensity and morphologic change that precedes or coincides with it are under way.

Acknowledgments

The authors thank their Devers Eye Institute colleagues Brad Fortune and Grant Cull for their assistance with the implementation of the FoBMO sectoral axon count methodology. CB thanks John Crabb, of the Cleveland Clinic, whose prelim-

inary proteomic findings suggested that myelin-related alterations were present in NHP early EG.

Supported by NIH R01 EY011610 (CFB), NIH R01 EY029087 (NMA, CFB) American Glaucoma Society (CFB), Sears Trust (CFB), Bright Focus (PC, HY), Alcon Research Institute (PC, CFB), and Legacy Good Samaritan Foundation–Devers Eye Institute Endowment (CFB).

Disclosure: **P. Chaudhary**, None; **H. Lockwood**, None; **C. Stowell**, None; **E. Bushong**, None; **J. Reynaud**, None; **H. Yang**, None; **S.K. Gardiner**, None; **G. Wiliams**, None; **I. Williams**, None; **M. Ellisman**, None; **N. Marsh-Armstrong**, None; **C. Burgoyne**, Heidelberg Engineering (F, R), Reichert (F)

References

1. Jakobs TC, Libby RT, Ben Y, John SW, Masland RH. Retinal ganglion cell degeneration is topological but not cell type specific in DBA/2J mice. *J Cell Biol*. 2005;171(2):313–325.
2. Howell GR, Libby RT, Jakobs TC, et al. Axons of retinal ganglion cells are insulted in the optic nerve early in DBA/2J glaucoma. *J Cell Biol*. 2007;179(7):1523–1537.
3. Johnson EC, Jia L, Cepurna WO, Doser TA, Morrison JC. Global changes in optic nerve head gene expression after exposure to elevated intraocular pressure in a rat glaucoma model. *Invest Ophthalmol Vis Sci*. 2007;48(7):3161–3177.
4. Minckler DS, Tso MO, Zimmerman LE. A light microscopic, autoradiographic study of axoplasmic transport in the optic nerve head during ocular hypotony, increased intraocular pressure, and papilledema. *Am J Ophthalmol*. 1976;82(5):741–757.
5. Minckler DS, Bunt AH, Johanson GW. Orthograde and retrograde axoplasmic transport during acute ocular hypertension in the monkey. *Invest Ophthalmol Vis Sci*. 1977;16(5):426–441.
6. Minckler DS, Bunt AH, Klock IB. Radioautographic and cytochemical ultrastructural studies of axoplasmic transport in the monkey optic nerve head. *Invest Ophthalmol Vis Sci*. 1978;17(1):33–50.
7. Quigley HA, Addicks EM, Green WR, Maumenee AE. Optic nerve damage in human glaucoma. II. The site of injury and susceptibility to damage. *Arch Ophthalmol*. 1981;99(4):635–649.
8. Burgoyne CF. The non-human primate experimental glaucoma model. *Exp Eye Res*. 2015;141:57–73.
9. Yang H, Downs JC, Girkin C, et al. 3-D histomorphometry of the normal and early glaucomatous monkey optic nerve head: lamina cribrosa and peripapillary scleral position and thickness. *Invest Ophthalmol Vis Sci*. 2007;48(10):4597–4607.
10. Yang H, Downs JC, Bellezza A, Thompson H, Burgoyne CF. 3-D histomorphometry of the normal and early glaucomatous monkey optic nerve head: prelaminar neural tissues and cupping. *Invest Ophthalmol Vis Sci*. 2007;48(11):5068–5084.
11. Yang H, Downs JC, Sigal IA, Roberts MD, Thompson H, Burgoyne CF. Deformation of the normal monkey optic nerve head connective tissue after acute IOP elevation within 3-D histomorphometric reconstructions. *Invest Ophthalmol Vis Sci*. 2009;50(12):5785–5799.
12. Yang H, Williams G, Downs JC, et al. Posterior (outward) migration of the lamina cribrosa and early cupping in monkey experimental glaucoma. *Invest Ophthalmol Vis Sci*. 2011;52(10):7109–7121.
13. Yang H, Ren R, Lockwood H, et al. The connective tissue components of optic nerve head cupping in monkey experimental glaucoma part 1: global change. *Invest Ophthalmol Vis Sci*. 2015;56(13):7661–7678.
14. Yang H, Reynaud J, Lockwood H, et al. The connective tissue phenotype of glaucomatous cupping in the monkey eye—clinical and research implications. *Prog Retin Eye Res*. 2017;59:1–52.
15. Yang H, Reynaud J, Lockwood H, et al. 3D histomorphometric reconstruction and quantification of the optic nerve head connective tissues. *Methods Mol Biol*. 2018;1695:207–267.
16. Burgoyne CF, Downs JC, Bellezza AJ, Suh JK, Hart RT. The optic nerve head as a biomechanical structure: a new paradigm for understanding the role of IOP-related stress and strain in the pathophysiology of glaucomatous optic nerve head damage. *Prog Retin Eye Res*. 2005;24(1):39–73.
17. Downs JC, Roberts MD, Burgoyne CF. Mechanical environment of the optic nerve head in glaucoma. *Optom Vis Sci*. 2008;85(6):425–435.
18. Kwun Y, Han JC, Kee C. Comparison of lamina cribrosa thickness in normal tension glaucoma patients with unilateral visual field defect. *Am J Ophthalmol*. 2015;159(3):512–518.e1.
19. Fard MA, Afzali M, Abdi P, et al. Optic nerve head morphology in nonarteritic anterior ischemic optic neuropathy compared to open-angle glaucoma. *Invest Ophthalmol Vis Sci*. 2016;57(11):4632–4640.
20. Han JC, Choi DY, Kwun YK, Suh W, Kee C. Evaluation of lamina cribrosa thickness and depth in ocular hypertension. *Jpn J Ophthalmol*. 2016;60(1):14–19.
21. Sharpe GP, Danthurebandara VM, Vianna JR, et al. Optic disc hemorrhages and laminar disinsertions in glaucoma. *Ophthalmology*. 2016;123(9):1949–1956.
22. Fard MA, Moghimi S, Sahraian A, Ritch R. Optic nerve head cupping in glaucomatous and non-glaucomatous optic neuropathy. *Br J Ophthalmol*. 2019;103(3):374–378.
23. Moghimi S, Zangwill LM, Manalastas PIC, et al. Association between lamina cribrosa defects and progressive retinal nerve fiber layer loss in glaucoma. *JAMA Ophthalmol*. 2019;137(4):425–433.
24. Kim JA, Kim TW, Lee EJ, Girard MJA, Mari JM. Comparison of lamina cribrosa morphology in eyes with ocular hypertension and normal-tension glaucoma. *Invest Ophthalmol Vis Sci*. 2020;61(4):4.
25. Lee SH, Kim TW, Lee EJ, Girard MJA, Mari JM. Focal lamina cribrosa defects are not associated with steep lamina cribrosa curvature but with choroidal microvascular dropout. *Sci Rep*. 2020;10(1):6761.
26. Radius RL, Pederson JE. Laser-induced primate glaucoma. II. *Histopathol Arch Ophthalmol*. 1984;102(11):1693–1698.
27. Fortune B, Wang L, Bui BV, Burgoyne CF, Cioffi GA. Idiopathic bilateral optic atrophy in the rhesus macaque. *Invest Ophthalmol Vis Sci*. 2005;46(11):3943–3956.
28. Burton EV, Greenberg BM, Frohman EM. Optic neuritis: a mechanistic view. *Pathophysiology*. 2011;18(1):81–92.
29. Yang D, Fu J, Hou R, et al. Optic neuropathy induced by experimentally reduced cerebrospinal fluid pressure in monkeys. *Invest Ophthalmol Vis Sci*. 2014;55(5):3067–3073.
30. Ing E, Ivers KM, Yang H, et al. Cupping in the monkey optic nerve transection model consists of prelaminar tissue thinning in the absence of posterior laminar deformation. *Invest Ophthalmol Vis Sci*. 2016;57(6):2914–2927.
31. Fadda G, Flanagan EP, Cacciaguerra L, et al. Myelitis features and outcomes in CNS demyelinating disorders: comparison between multiple sclerosis, MOGAD, and AQP4-IgG-positive NMOSD. *Front Neurol*. 2022;13:1011579.
32. Ciapă MA, Şalaru DL, Stătescu C, Sascău RA, Bogdănici CM. Optic neuritis in multiple sclerosis—a review of molecular mechanisms involved in the degenerative process. *Curr Issues Mol Biol*. 2022;44(9):3959–3979.

Investigative Ophthalmology & Visual Science

33. Ortiz GG, Torres-Mendoza BMG, Ramírez-Jirano J, et al. Genetic basis of inflammatory demyelinating diseases of the central nervous system: multiple sclerosis and neuromyelitis optica spectrum. *Genes (Basel)*. 2023;14(7):1319.
34. Bunt-Milam AH, Dennis MB, Jr, Bensinger RE. Optic nerve head axonal transport in rabbits with hereditary glaucoma. *Exp Eye Res*. 1987;44(4):537–551.
35. Chidlow G, Ebneter A, Wood JP, Casson RJ. The optic nerve head is the site of axonal transport disruption, axonal cytoskeleton damage and putative axonal regeneration failure in a rat model of glaucoma. *Acta Neuropathol*. 2011;121(6):737–751.
36. Tribble JR, Otmani A, Kokkali E, Lardner E, Morgan JE, Williams PA. Retinal ganglion cell degeneration in a rat magnetic bead model of ocular hypertensive glaucoma. *Transl Vis Sci Technol*. 2021;10(1):21.
37. Risner ML, Pasini S, McGrady NR, Calkins DJ. Bax contributes to retinal ganglion cell dendritic degeneration during glaucoma. *Mol Neurobiol*. 2022;59(3):1366–1380.
38. Chaudhary P, Marracci G, Yu X, Galipeau D, Morris B, Bourdette D. Lipoic acid decreases inflammation and confers neuroprotection in experimental autoimmune optic neuritis. *J Neuroimmunol*. 2011;233(1–2):90–96.
39. Hartley MD, Banerji T, Tagge IJ, et al. Myelin repair stimulated by CNS-selective thyroid hormone action. *JCI Insight*. 2019;4(8):e126329.
40. Sapko K, Jamroz-Wiśniewska A, Rejdak K. Novel drugs in a pipeline for progressive multiple sclerosis. *J Clin Med*. 2022;11(12):3342.
41. Yang JH, Rempe T, Whitmire N, Dunn-Pirio A, Graves JS. Therapeutic advances in multiple sclerosis. *Front Neurol*. 2022;13:824926.
42. Bresciani G, Manai F, Davinelli S, Tucci P, Saso L, Amadio M. Novel potential pharmacological applications of dimethyl fumarate—an overview and update. *Front Pharmacol*. 2023;14:1264842.
43. Andrade S, Nunes D, Dabur M, Ramalho MJ, Pereira MC, Loureiro JA. Therapeutic potential of natural compounds in neurodegenerative diseases: insights from clinical trials. *Pharmaceutics*. 2023;15(1):212.
44. Amin M, Hersh CM. Updates and advances in multiple sclerosis neurotherapeutics. *Neurodegener Dis Manag*. 2023;13(1):47–70.
45. Smith MA, Plyler ES, Dengler-Crish CM, Meier J, Crish SD. Nodes of Ranvier in glaucoma. *Neuroscience*. 2018;390:104–118.
46. Chaudhary P, Stowell C, Reynaud J, et al. Optic nerve head myelin-related protein, GFAP, and Iba1 alterations in nonhuman primates with early to moderate experimental glaucoma. *Invest Ophthalmol Vis Sci*. 2022;63(11):9.
47. Reynaud J, Cull G, Wang L, et al. Automated quantification of optic nerve axons in primate glaucomatous and normal eyes—method and comparison to semi-automated manual quantification. *Invest Ophthalmol Vis Sci*. 2012;53(6):2951–2959.
48. Pohlman RM, Turney MR, Wu PH, Brace CL, Ziemlewicz TJ, Varghese T. Two-dimensional ultrasound-computed tomography image registration for monitoring percutaneous hepatic intervention. *Med Phys*. 2019;46(6):2600–2609.
49. Bushong EA, Phan S, Ellisman MH. Using x-ray microscopy to increase targeting accuracy in serial block-face scanning electron microscopy. In: Wacker I, Hummel E, Burgold S, Schröder R, eds. *Volume Microscopy: neuromethods*. Vol. 155. New York, NY: Humana; 2020.
50. Wilke SA, Antonios JK, Bushong EA, et al. Deconstructing complexity: serial block-face electron microscopic analysis of the hippocampal mossy fiber synapse. *J Neurosci*. 2013;33(2):507–522.
51. Kremer JR, Mastronarde DN, McIntosh JR. Computer visualization of three-dimensional image data using IMOD. *J Struct Biol*. 1996;116(1):71–76.
52. Lockwood H, Reynaud J, Gardiner S, et al. Lamina cribrosa microarchitecture in normal monkey eyes part 1: methods and initial results. *Invest Ophthalmol Vis Sci*. 2015;56(3):1618–1637.
53. Reynaud J, Lockwood H, Gardiner SK, Williams G, Yang H, Burgoyne CF. Lamina cribrosa microarchitecture in monkey early experimental glaucoma: global change. *Invest Ophthalmol Vis Sci*. 2016;57(7):3451–3469.
54. Moore DF. *Applied Survival Analysis Using R. Use R!*. Switzerland: Springer International Publishing; 2016.
55. Fortune B, Cull G, Reynaud J, Wang L, Burgoyne CF. Relating retinal ganglion cell function and retinal nerve fiber layer (RNFL) retardance to progressive loss of RNFL thickness and optic nerve axons in experimental glaucoma. *Invest Ophthalmol Vis Sci*. 2015;56(6):3936–3944.
56. Fortune B, Hardin C, Reynaud J, et al. Comparing optic nerve head rim width, rim area, and peripapillary retinal nerve fiber layer thickness to axon count in experimental glaucoma. *Invest Ophthalmol Vis Sci*. 2016;57(9):OCT404–OCT412.
57. Harwerth RS, Vilupuru AS, Rangaswamy NV, Smith EL, III. The relationship between nerve fiber layer and perimetry measurements. *Invest Ophthalmol Vis Sci*. 2007;48(2):763–773.
58. Cull GA, Reynaud J, Wang L, Cioffi GA, Burgoyne CF, Fortune B. Relationship between orbital optic nerve axon counts and retinal nerve fiber layer thickness measured by spectral domain optical coherence tomography *Invest Ophthalmol Vis Sci*. 2012;53(12):7766–7773, doi:10.1167/iovs.12-10752. Erratum in: *Invest Ophthalmol Vis Sci*. 2014 Apr;55(4):2619–20. PMID: 23125332; PMCID: PMC3506054.
59. Minckler DS, McLean IW, Tso MO. Distribution of axonal and glial elements in the rhesus optic nerve head studied by electron microscopy. *Am J Ophthalmol*. 1976;82(2):179–187.
60. Gaasterland D, Tanishima T, Kuwabara T. Axoplasmic flow during chronic experimental glaucoma. 1. Light and electron microscopic studies of the monkey optic nervehead during development of glaucomatous cupping. *Invest Ophthalmol Vis Sci*. 1978;17(9):838–846.
61. Quigley HA, Green WR. The histology of human glaucoma cupping and optic nerve damage: clinicopathologic correlation in 21 eyes. *Ophthalmology*. 1979;86(10):1803–1830.
62. Quigley HA, Addicks EM, Green WR. Optic nerve damage in human glaucoma. III. Quantitative correlation of nerve fiber loss and visual field defect in glaucoma, ischemic neuropathy, papilledema, and toxic neuropathy. *Arch Ophthalmol*. 1982;100(1):135–146.
63. Renner M, Stute G, Alzureiqi M, et al. Optic nerve degeneration after retinal ischemia/reperfusion in a rodent model. *Front Cell Neurosci*. 2017;11:254.
64. Korneva A, Schaub J, Jefferys J, et al. A method to quantify regional axonal transport blockade at the optic nerve head after short term intraocular pressure elevation in mice. *Exp Eye Res*. 2020;196:108035.
65. Mills EA, Davis CH, Bushong EA, et al. Astrocytes phagocytose focal dystrophies from shortening myelin segments in the optic nerve of Xenopus laevis at metamorphosis. *Proc Natl Acad Sci USA*. 2015;112(33):10509–10514.
66. Nguyen JV, Soto I, Kim KY, et al. Myelination transition zone astrocytes are constitutively phagocytic and have synuclein dependent reactivity in glaucoma. *Proc Natl Acad Sci USA*. 2011;108(3):1176–1181.

Investigative Ophthalmology & Visual Science

67. Davis CH, Kim KY, Bushong EA, et al. Transcellular degradation of axonal mitochondria. *Proc Natl Acad Sci USA*. 2014;111(26):9633–9638.
68. De Moraes CG, John SWM, Williams PA, Blumberg DM, Cioffi GA, Liebmann JM. Nicotinamide and pyruvate for neuroenhancement in open-angle glaucoma: a phase 2 randomized clinical trial. *JAMA Ophthalmol*. 2022;140(1):11–18.
69. Williams PA, Harder JM, Foxworth NE, et al. Vitamin B_3 modulates mitochondrial vulnerability and prevents glaucoma in aged mice. *Science*. 2017;355(6326):756–760.
70. Williams PA, Marsh-Armstrong N, Howell GR; Lasker/IRRF Initiative on Astrocytes and Glaucomatous Neurodegeneration Participants. Neuroinflammation in glaucoma: a new opportunity. *Exp Eye Res*. 2017;157:20–27.
71. Morgan JE, Jeffery G, Foss AJ. Axon deviation in the human lamina cribrosa. *Br J Ophthalmol*. 1998;82(6):680–683.
72. Radius RL, Anderson DR. The course of axons through the retina and optic nerve head. *Arch Ophthalmol*. 1979; 97(6):1154–1158.
73. Minckler DS. The organization of nerve fiber bundles in the primate optic nerve head. *Arch Ophthalmol*. 1980; 98(9):1630–1636.
74. Ogden TE. Nerve fiber layer of the macaque retina: retinotopic organization. *Invest Ophthalmol Vis Sci*. 1983; 24(1):85–98.
75. Fitzgibbon T, Taylor SF. Retinotopy of the human retinal nerve fibre layer and optic nerve head. *J Comp Neurol*. 1996;375(2):238–251.

Investigative Ophthalmology & Visual Science